ATLAS CONF Note

ATLAS-CONF-2022-047

4th July 2022

Measurements of $Z\gamma$ + jets differential cross sections in pp collisions at $\sqrt{s} = 13$ TeV with the ATLAS detector

The ATLAS Collaboration

Differential cross-section measurements of $Z\gamma$ production in association with hadronic jets are presented, using the full Run-2 proton-proton dataset of 139 fb^{-1} produced by the LHC at $\sqrt{s} = 13$ TeV and collected by the ATLAS detector. Distributions are measured using events in which the Z boson decays leptonically and the photon is predominantly radiated off the initial state quarks. Both one- and two-dimensional observables are considered, including observables sensitive to the hard scatter in the event and observable which probe additional soft and collinear radiation. The measurements are compared to different Standard Model predictions, both parton-shower Monte-Carlo simulation and fixed-order QCD calculations. General good agreement is observed between data and state-of-the art theoretical next-to-next-leading-order predictions MATRIX/MiNNLO$_{PS}$ and with MadGraph5_aMC@NLO and Sherpa multileg next-to-leading order generators.

ATLAS-CONF-2022-047
20 July 2022

1 Introduction

Precision measurements at the Large Hadron Collider (LHC) [1, 2] play a crucial role in the study of the Standard Model (SM), especially in the absence of clear indications of physics beyond the SM. An important process in this context is the production of colour singlets, such as a Z boson and a photon ($Z\gamma$), in association with QCD radiation, that are sensitive to hadronic activity through kinematic recoil. Differential distributions can be used to test models that are used as inputs in determining parton density functions (PDF) [3], Parton Shower (PS) predictions [4], or fixed-order QCD calculations of differential distributions with resummation of Sudakov logarithms [5, 6].

In phase-space regions where the transverse momentum (q_T) of the system is much smaller than the mass of the colour singlet M, which can stand for the $Z\gamma$ (or Z) system, fixed order QCD calculations are dominated by Sudakov logarithm terms caused by soft and collinear emission of the order of $\alpha_s^n \ln^m(q_T/M)$, where n is the fixed order considered and m the next one. These terms are usually treated by resummation [5] and can give very precise predictions at next-to-leading logarithmic (NLL) and up to next-to-next-to-next-to-leading logarithmic (N3LL) [7]. It is important to test these resummation models in phase-space regions where the logarithm terms dominate, meaning where the hard scale of the process (Q) is much larger than the differential observable (p) considered. This phase-space of interest can be probed by measuring an observable sensitive to the hard scatter as a function of another observable which probes additional soft radiation. This is done with 2D distributions including a "*hard variable*" and a "*resolution variable*". "*Hard variable*" denotes an observable that represents the hard scale of the process, which is non-zero at leading order (LO); e.g. p_T^Z , p_T^γ, $m_{Z\gamma}$, and their linear combinations. "*Resolution variable*" refers to an observable that is sensitive to additional, soft or collinear, QCD radiation; these observables are zero at LO and take non-zero values only beyond LO, e.g $p_T^{Z\gamma}$ or N_{jet}.

Measurements of $Z\gamma$ has been shown able to probe important parameters of the SM predictions [8, 9], by looking for discrepancies from the SM predictions in the differential cross sections. Such measurements can also be used to search for physics beyond the SM. One example is given by the axion-like particles (ALPs) [10], which are introduced to solve the strong CP problem and are considered as Dark Matter candidates [11]. However, studies done at LEP [12–14], the Tevatron [15, 16], and the LHC [17–19] have not found any evidence of new physics so far. All these measurements did not include any dedicated study of the jet activity.

The analysis presented here studies differential cross sections of QCD-related observables associated with the $Z\gamma$ process. The analysis uses the full dataset of proton-proton (pp) collisions, produced by the LHC during the 2015−2018 Run-2 at a centre-of-mass energy of $\sqrt{s}$ = 13 TeV, and recorded by the ATLAS detector. The study builds on an analysis performed by ATLAS at $\sqrt{s}$ = 13 TeV [18], which focused on more inclusive observables. Only Z bosons decaying into pairs of either electrons or muons, $Z\gamma \to \ell^+\ell^-\gamma$ (with $\ell = e, \mu$), are considered. This is both due to the possibility to fully reconstruct the final state, and a relatively large cross section with a small background. Events are selected by requiring the invariant mass of the two leptons, $m_{\ell\ell}$, to be greater than 40 GeV, and the sum of the mass of the dilepton system and the mass of the $\ell\ell\gamma$ system, $m_{\ell\ell} + m_{\ell\ell\gamma}$, to be greater than 182 GeV. These selections define a phase-space that is enriched in photons from initial state radiation (ISR), such as shown in Fig. 1 (a), with reduced contributions from photons radiated off leptons, called final state radiation (FSR), shown in Fig. 1 (b).

Differential cross-sections of $Z\gamma$ production and jets activity provide sensitive tests of QCD predictions. Data are compared to generators with multileg matrix elements with parton shower and hadronization,

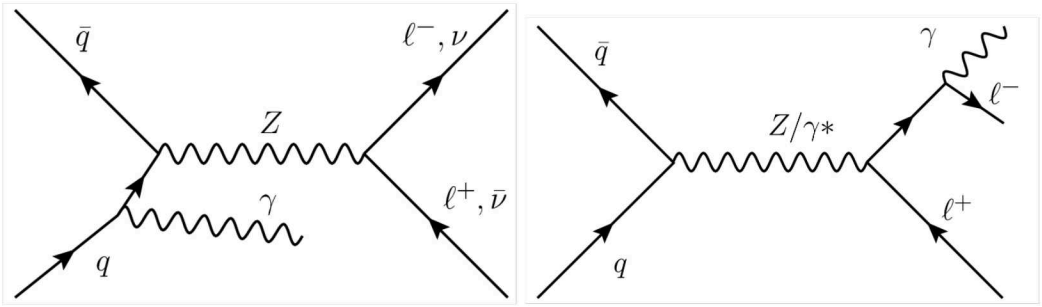

Figure 1: Diagrams for $Z\gamma$ production via the ISR process (a), $\ell\ell\gamma$ production via the FSR process (b).

as well as to next-to-next-to-leading order (NNLO) predictions which have recently became available. Several parton shower Monte Carlo (MC) models are considered with different levels of precision. These include SHERPA 2.2.4 and 2.2.11 [20] , respectively at LO and next-to-leading order (NLO) precision, `MadGraph` at NLO [21] and MiNNLO$_{PS}$ at NNLO with PS matching [22, 23] . Additionally, fixed order QCD calculations are also considered, obtained with the MATRIX [24, 25] software at NNLO precision. Differential measurements are performed both in one and in two dimensions, using distributions with and without jet related observables.

2 The ATLAS detector

The ATLAS experiment [26] at the LHC is a multipurpose particle detector with a forward–backward symmetric cylindrical geometry and a near 4π coverage in solid angle.[1] It consists of an inner tracking detector (ID) surrounded by a thin superconducting solenoid providing a 2 T axial magnetic field, electromagnetic (ECAL) and hadron calorimeters, and a muon spectrometer (MS). The inner tracking detector covers the pseudorapidity range $|\eta| < 2.5$. It consists of silicon pixel, silicon microstrip, and transition radiation tracking detectors. Lead/liquid-argon (LAr) sampling calorimeters provide electromagnetic (EM) energy measurements with high granularity. A steel/scintillator-tile hadron calorimeter covers the central pseudorapidity range ($|\eta| < 1.7$). The endcap and forward regions are instrumented with LAr calorimeters for both the EM and hadronic energy measurements up to $|\eta| = 4.9$. The muon spectrometer surrounds the calorimeters and is based on three large superconducting air-core toroidal magnets with eight coils each. The field integral of the toroids ranges between 2.0 and 6.0 T m across most of the detector. The muon spectrometer includes a system of precision tracking chambers and fast detectors for triggering. A two-level trigger system is used to select events. The first-level trigger is implemented in hardware and uses a subset of the detector information to accept events at a rate below 100 kHz. This is followed by a software-based trigger that reduces the accepted event rate to 1 kHz on average depending on the data-taking conditions. An extensive software suite [27] is used in the

[1] ATLAS uses a right-handed coordinate system with its origin at the nominal interaction point (IP) in the centre of the detector and the z-axis along the beam pipe. The x-axis points from the IP to the centre of the LHC ring, and the y-axis points upwards. Cylindrical coordinates (r, ϕ) are used in the transverse plane, ϕ being the azimuthal angle around the z-axis. The pseudorapidity is defined in terms of the polar angle θ as $\eta = -\ln\tan(\theta/2)$. Angular distance is measured in units of $\Delta R \equiv \sqrt{(\Delta\eta)^2 + (\Delta\phi)^2}$.

reconstruction and analysis of real and simulated data, in detector operations, and in the trigger and data acquisition systems of the experiment.

3 Data and simulated samples

The data used in this analysis were produced by the LHC in pp collisions in Run 2, and after passing the data quality criteria [28], the total integrated luminosity recorded by the ATLAS detector is 139 fb^{-1}. The uncertainty in the luminosity is 1.7% [29] and is obtained from measurements with the LUCID-2 detector [30].

Three different Monte Carlo samples are used to simulate the $Z\gamma$ process. The nominal sample is generated using the program Sherpa 2.2.11 with matrix elements up to one additional parton at NLO and with up to three additional partons at LO. The PS merging is performed with MEPS@NLO [31–34]. The PDF set is `NNPDF3.0nnlo` [35], with an additional set of tuned PS parameters developed by the Sherpa authors. Frixione isolation [36] is applied to the photon with the parameter choices $\delta_0 = 0.1$, $\epsilon = 0.1$ and $n = 2$. This sample requires the transverse momentum of the photon, p_{T}^{γ}, to be greater than 7 GeV. Throughout the paper the signal estimate refers to this sample unless it is otherwise specified.

A second sample has been produced using the program Sherpa 2.2.4, with matrix elements up to three additional partons at leading order (LO) in QCD. The PS merging is performed with MEPS@NLO. The PDF set used is `NNPDF3.0nnlo`. The sample is sliced in p_{T}^{γ}, to enhance the statistics at high transverse momenta. In the generation, p_{T}^{γ} is required to be larger than 7 GeV. Frixion isolation is also applied to this sample, with the same cuts as the Sherpa 2.2.11 sample.

An third sample is generated using the program MadGraph5_aMC@NLO 2.3.3 [21] containing NLO matrix elements with up to one extra parton, using the `NNPDF3.0nlo` _as_0118 PDF set [37]. This sample has the same Frixione isolation cuts as the Sherpa samples.

Simulated samples of the electroweak production of $Z\gamma$ are generated using the program MadGraph5_aMC@NLO 2.6.5 [21] at leading order (LO) accuracy, using the `NNPDF3.0lo` PDF set [37]. It is interfaced with Pythia 8.240 [38] for parton showering, hadronisation, and underlying events.

The main backgrounds to the signal arise from Z boson produced in association with jets, top pair and single top produced in association with photons, diboson and triboson events, and multiple pp interactions, called pile-up events.

The Z boson in association with jets (Z + jets) MC samples used in this analysis is generated using the PowhegBox v1 MC generator [39–42], with NLO accuracy of the hard-scattering processes. It is interfaced to Pythia8.186 [38] for the modelling of the PS, hadronisation, and underlying events, with parameters set according to the AZNLO tune [43]. The `CT10` PDF set [44] is used for the hard-scattering processes, whereas the `CTEQ6L1` PDF set [45] is used for the PS. This background is normalized to the internal cross section from the generator.

The MC samples of the production of one or two top quarks and a photon ($t\bar{t}\gamma$ and $tW\gamma$) is generated using the program MadGraph5_aMC@NLO v2.3.3 [21] at LO with the `NNPDF2.3lo` [37] PDF set. The events are interfaced with Pythia8.212 [46] using the A14 tune [47] and the `NNPDF2.3lo` PDF set. These samples are normalised to their NLO cross section [48, 49].

Process	Generator	Order	PDF Set	PS/UE/MPI
$Z\gamma$+jets	Sherpa 2.2.11	0,1j @NLO+2,3,4j @LO	NNPDF3.0nnlo	Sherpa 2.2.11
$Z\gamma$+jets	Sherpa 2.2.4	0,1,2,3 j@ LO	NNPDF3.0nnlo	Sherpa 2.2.4
$Z\gamma$+jets	MadGraph	0,1j @NLO	NNPDF3.0nlo _as_0118	Pythia8.212
Z + jets	PowhegBox	0j @NLO	CT10	Pythia8.186
$t\bar{t}\gamma$/ $tW\gamma$	MadGraph5_aMC@NLO	LO	NNPDF2.3lo	Pythia8.212
$ZZ \to \ell\ell\ell\ell$/ $W^{\pm}Z \to \ell\ell\ell\nu$	Sherpa 2.2.2	0,1j @NLO + 2,3j @LO	NNPDF3.0nnlo	Sherpa 2.2.2
$WZ\gamma$/ $WW\gamma$	Sherpa 2.2.11	0j @NLO + 1,2j @LO	N30NNLO	Sherpa 2.2.5
EW $Z\gamma$	MadGraph	0j @LO	NNPDF3.0lo	Pythia 8.240

Table 1: Summary of MC samples used in the analysis.

The MC samples of diboson processes, such as $ZZ \to \ell\ell\ell\ell$ and $W^{\pm}Z \to \ell\ell\ell\nu$, are generated with Sherpa 2.2.2 at NLO with up to one additional parton using the NNPDF3.0nnlo NNLO PDF set. $WZ\gamma$ and $WW\gamma$ also constitute a small background and are produced with Sherpa 2.2.11 at NLO with zero jets, using the N30NNLO PDF set. The multiboson background are normalized to the Sherpa cross section.

For all these MC samples, pile-up from additional pp collisions in the same and neighbouring bunch crossings is simulated by overlaying each MC event with a variable number of simulated inelastic pp collisions generated using Pythia 8.186 with the ATLAS set of tuned parameters for minimum bias events (A2 tune) [50]. The MC events are weighted ("pile-up reweighting") to reproduce the distribution of the average number of interactions per bunch crossing observed in the data. All the samples of generated events were passed through the Geant 4-based [51] ATLAS detector- and trigger-simulation programs [52]. They were reconstructed and analysed by the same program chain as the data.

Table 1 gives an overview of the generators used in this analysis, their precision in QCD and the PDF set used.

3.1 Additional theory predictions

NNLO predictions matched to PS are compared to the results presented in Section 9. These predictions are taken from Ref. [23], where PowhegBox [53] is used to generate NLO events with a NNLO extension based on the MiNNLO$_{PS}$ [22] method. This method has been extended to genuine $2 \to 2$ processes that include the NNLO correction directly during generation. Photon infrared-safe predictions are obtained by imposing the same Frixione isolation parameters as for the nominal MC, Sherpa 2.2.11. The central renormalization and factorization scales are set to $\mu_{R,0} = \mu_{F,0} = m_{\ell\ell\gamma}$. Events are generated using the NNPDF3.0nnlo PDF set with the strong coupling constant set to $\alpha_s(m_Z) = 0.118$.

Additionally, fixed order QCD calculations are also considered using the software MATRIX [24, 25], with CT14nnlo PDF [54]. Frixione isolation parameters are the same as in the nominal MC sample, Sherpa 2.2.11. MATRIX predictions are obtained at Born level (parton level), since no QED radiation is present, while the results obtained with the Sherpa 2.2.11 MC are at particle level. For this reason corrections are applied to the fixed order calculations to compare the calculations with the results. These corrections are calculated by comparing Born level leptons to "*dressed* leptons". Leptons are "dressed", when they are corrected for collinear photon radiation: the four-momenta of photons not from hadrons decays that fall within $\Delta R < 0.1$ of a lepton are added to its four-momentum. Additionally, MATRIX does not include non-perturbative effects, and corrections are applied to compare to the measurements. These corrections are obtained by calculating the ratio of the MC cross section with and without hadronization effects turned

on. The MC sample is generated with MadGraph5_aMC@NLO with up to one extra parton at NLO in the matrix element, and then interfaced with Pythia8 [46], using the ATLAS tune A14 [47].

4 Event selection

Events are selected if they contain at least one reconstructed pp vertex with at least two associated tracks with $p_{\mathrm{T}} > 400$ MeV. In events with multiple vertices, the one with the highest $\sum p_{\mathrm{T}}^2$ of associated tracks is selected. Candidate events must also pass at least one unprescaled single muon or single electron trigger [55, 56]. In the 2015 data taking period, the lowest p_{T} threshold was 24 GeV for the electron trigger, and 20 GeV for the muon trigger. During the 2016−2018 data taking period, these thresholds were both increased to 26 GeV and tighter isolation criteria were applied, to compensate for the increase in instantaneous luminosity. Triggers with higher p_{T} threshold, but looser isolation, are also considered to further increase the total data taking efficiency.

4.1 Lepton, photon, and jet selections

Photons and electrons are reconstructed starting from energy clusters in the ECAL. Electron candidates are required to have a matching track in the ID. Photon candidates must have $|\eta| < 2.37$ and $p_{\mathrm{T}} > 30$ GeV, while electron candidates must have $|\eta| < 2.47$ and $p_{\mathrm{T}} > 25$ GeV. Both electron and photon candidates are rejected if they lie in the transition region between the barrel and the end cap of the calorimeter ($1.37 < |\eta| < 1.52$). Electrons are identified based on a *likelihood* function that uses shower shape variables in the ECAL, track variables, and the quality of the track-cluster matching as inputs. Electrons are required to pass the *Medium* criteria, as described in Ref. [57]. Photons are identified based on shower shape variables in the ECAL and are required to pass the *Tight* criteria [57]. Photons are classified as *converted* to electron-positron pairs if the ECAL cluster is matched to a conversion vertex formed by oppositely charged tracks, or by a single track consistent with having originated from a photon conversion. Photon candidates are classified as *unconverted* if it is not possible to match clusters and tracks. Both types of photons are used in this analysis. The photon and electron energy scale is calibrated using $Z \to ee$ events, as described in Ref. [57].

Muons are reconstructed by matching the tracks in the MS with the ones in the ID. The momentum is obtained by combining the MS measurement corrected by the energy deposited in the calorimeter, and the measurement in the ID. Muon candidates are also required to pass the *Medium* identification criteria, as described in Ref. [58]. This criteria is based on the number of hits matched to the tracks reconstructed both in the ID and in the MS, and on the significance of the compatibility of the measurements of the transverse momentum in the ID and in the MS. Muon candidates are required to have $|\eta| < 2.5$ and $p_{\mathrm{T}} > 25$ GeV.

Electrons and muons must be compatible with originating from the primary vertex. This requirement is fulfilled by demanding that the transverse impact parameter (d_0) relative to the beam position divided by its uncertainty ($\sigma(d_0)$), i.e. the significance, satisfy $|d_0/\sigma(d_0)| < 5$ for electrons and $|d_0/\sigma(d_0)| < 3$ for muons. Additionally, for both electrons and muons, the longitudinal impact parameter (z_0) must satisfy $|z_0 \sin\theta| < 0.5$ mm from the primary interaction vertex.

Leptons and photons are required to be isolated, i.e. without additional activity in their proximity. Isolation requirements are based on tracking information and calorimeter clusters. The isolation variable $p_{\mathrm{T}}^{\mathrm{iso}}$ is computed as the $\sum p_{\mathrm{T}}$ of the near-by tracks with $p_{\mathrm{T}} > 1$ GeV, excluding tracks associated to the lepton or

photon candidate. The variable $E_{\mathrm{T}}^{\mathrm{iso}}$ is obtained as the scalar sum of the transverse energy of topological clusters. $E_{\mathrm{T}}^{\mathrm{iso}}$ is corrected for the energy deposited by the photon or lepton candidate and the contribution from the underlying event and pile-up [59, 60].

Photons must pass an isolation criteria as described in Ref. [57] where: $p_{\mathrm{T}}^{\mathrm{iso}}/E_{\mathrm{T}} < 0.05$ and $E_{\mathrm{T}}^{\mathrm{iso}}/E_{\mathrm{T}} < 0.065$, in a cone of radius $R = 0.2$ around the candidate photons. Electrons must satisfy $p_{\mathrm{T}}^{\mathrm{iso}}/p_{\mathrm{T}} < 0.15$ in a cone of varying radius up to $R = 0.2$ around the candidate electrons, and $E_{\mathrm{T}}^{\mathrm{iso}}/p_{\mathrm{T}} < 0.2$ in a cone of radius $R = 0.2$. Muons are required to be isolated [58] by requiring $p_{\mathrm{T}}^{\mathrm{iso}}/p_{\mathrm{T}} < 0.15$ in a cone of varying radius up to $R = 0.3$ ($R = 0.2$) for muons with p_{T} less (greater) than 50 GeV, and $E_{\mathrm{T}}^{\mathrm{iso}}/p_{\mathrm{T}} < 0.3$ in a fixed cone of radius $R = 0.2$.

Jets are reconstructed with the anti-k_t algorithm [61] with a radius parameter of $R = 0.4$, using a Particle Flow (PFlow) [62] procedure, with clusters of energy deposited in the calorimeter as inputs. Jets are calibrated and their energy is corrected to account for detector effects, using methods based on MC and in-situ techniques [63]. The mitigation of pile-up jets is obtained with the jet vertex tagger (JVT) [64], using the *Medium* working point applied to all jets with $p_{\mathrm{T}} < 60$ GeV and $|\eta| < 2.4$. Jets are required to have $p_{\mathrm{T}} > 30$ GeV if $|\eta| < 2.5$ or $p_{\mathrm{T}} > 50$ GeV if $|\eta| > 2.5$ to further suppress pile-up. Distributions with jets require $N_{\mathrm{Jet}} \geq 1$, unless it explicitly requires $N_{\mathrm{Jet}} \geq 2$ (e.g. m_{jj}).

Ambiguities in reconstruction between leptons, jets, and photons are resolved with the following overlap-removal procedure: jets are removed if they are found within $\Delta R < 0.4$ of a photon, or within $\Delta R < 0.2$ of an electron. Then leptons are removed if they are within $\Delta R < 0.4$ of a jet, while photons are removed if they are within $\Delta R < 0.4$ of a lepton. Finally, electrons are removed if they are within $\Delta R < 0.2$ of a muon.

4.2 Signal and control region definition

The Signal Region (SR) is defined by events with at least two opposite-sign (OS) same-flavor (SF) leptons and a photon. The leading lepton (with the highest transverse momentum) is required to have $p_{\mathrm{T}} > 30$ GeV. Events are also requested to have at least one photon with $p_{\mathrm{T}}^{\gamma} > 30$ GeV. Events are further selected by requiring $m_{\ell\ell} > 40$ GeV, to avoid low-mass resonances. FSR events are then suppressed by requiring that the sum of the invariant mass of the leptons combined with the invariant mass of the leptons and the photon is greater than twice the mass of the Z boson: $m_{\ell\ell} + m_{\ell\ell\gamma} > 182$ GeV. In the $m_{\ell\ell}$ vs $m_{\ell\ell\gamma}$ plane, this requirement is a diagonal straight line that separates FSR and ISR events since FSR events are expected to lie in the region with $m_{\ell\ell\gamma} \sim 90$ GeV and $m_{\ell\ell} < 90$ GeV (see Fig, 3 in Ref. [18]).
The $t\bar{t}\gamma$ background modelling is checked in a dedicated Control Region ($t\bar{t}\gamma$-CR) obtained by applying the SR requirement with the exception of the SF requirement that is replaced by different flavor (DF) leptons. The signature of this channel is then $e\mu\gamma$. All the other SR requirements are also applied. Table 2 shows a summary of these selection criteria.

Observable	Signal Region	$t\bar{t}\gamma$ Control Region
Number of signal leptons	2 Opposite Sign, Same Flavour	2 Opposite Sign, Different Flavour
Lepton	$p_{\mathrm{T}}(\ell_1) > 30$ GeV, $p_{\mathrm{T}}(\ell_2) > 25$ GeV	
Photon	≥ 1 photon with $p_{\mathrm{T}}^{\gamma} > 30$ GeV	
$m_{\ell\ell}$	> 40 GeV	
$m_{\ell\ell} + m_{\ell\ell\gamma}$	> 182 GeV	

Table 2: Summary of selection criteria used in this analysis.

5 Measured observables

Differential cross sections are measured for the following 1D observables:

- N_{Jet}, the number of jets
- $p_{\mathrm{T}}^{\mathrm{Jet1}}$ ($p_{\mathrm{T}}^{\mathrm{Jet2}}$), the transverse momentum of the leading jet (sub-leading jet)
- $p_{\mathrm{T}}^{\mathrm{Jet2}}/p_{T}^{\mathrm{Jet1}}$, the ratio of the p_{T} of the two leading jets
- $m_{\ell\ell\gamma j}$, the invariant mass of the lepton-photon-leading jet system
- m_{jj}, the invariant mass of the two leading jets
- H_{T}, the scalar sum of p_{T} of all jets, leptons, and photons
- $p_{\mathrm{T}}^{\gamma}/\sqrt{H_{\mathrm{T}}}$, the ratio between the p_{T} of the photon and the square root of H_{T}
- $\Delta\phi(\mathrm{Jet}, \gamma)$, the azimuthal angle difference between leading jet and leading photon
- $\Delta R(\ell, \ell)$, ΔR between the two leptons
- $p_{\mathrm{T}}^{\ell\ell}$, the transverse momentum of the vectorial sum of the two leptons.

QCD-sensitive 2D observables measured in this paper are:

- $p_{\mathrm{T}}^{\ell\ell\gamma}/m_{\ell\ell\gamma}$, the ratio of transverse momentum and the mass of the $Z\gamma$ system, in bins of the "*hard variable*" $m_{\ell\ell\gamma}$
- $p_{\mathrm{T}}^{\ell\ell} - p_{\mathrm{T}}^{\gamma}$ is measured in three different bins of the "*hard variable*" $p_{\mathrm{T}}^{\ell\ell} + p_{\mathrm{T}}^{\gamma}$
- $p_{\mathrm{T}}^{\ell\ell\gamma\mathrm{j}}$, the transverse momentum of the $Z\gamma j$ system, is measured in bins of the "*hard variable*" $p_{\mathrm{T}}^{\ell\ell\gamma}$

$p_{\mathrm{T}}^{\ell\ell} - p_{\mathrm{T}}^{\gamma}$, $p_{\mathrm{T}}^{\ell\ell} + p_{\mathrm{T}}^{\gamma}$, and $p_{\mathrm{T}}^{\ell\ell\gamma\mathrm{j}}$ are also measured inclusively.

Additionally, 2D observables sensitive to polarisation effects of the Z boson are considered [9]:

- $\cos\theta_{\mathrm{CS}}$, the cosine of the angle between the negative lepton and the lepton pair in the Collins-Soper (CS) frame [65] in bins of $p_{\mathrm{T}}^{\ell\ell}$
- ϕ_{CS}, the azimuthal angle between the negative lepton and the lepton pair in the CS frame in bins of $p_{\mathrm{T}}^{\ell\ell}$.

The observables sensitive to polarisation are estimated in the Collins-Soper frame where the Z-boson is at rest, and that is generally used in the literature when extracting angular coefficient of the Z-boson [8, 9].

In two dimensional distributions, to avoid the computational complication of unfolding a 2D distribution the first observable is unfolded in large bins of the second observable. The bins are chosen such that the migration effects in the second observable are negligible.

6 Background estimation

The main background to the $Z\gamma$ signal arises from Z + jets events, in which one of the jets is misidentified as a photon; this background is estimated using a data-driven method. Pile-up events, in which the leptons and the photon originate from two different pp interactions during the same bunch crossing, are also estimated using a data-driven method. Another large background, especially at high jet multiplicity, is $t\bar{t}\gamma$ production, where the top decay legs can also produce same-flavour leptons. The $t\bar{t}\gamma$ background is estimated using MC normalised to data in a dedicated CR. Other small backgrounds from triboson events, such as $WW\gamma$, $WZ\gamma$, and $ZZ\gamma$, that can also produce the same signature as the signal, and diboson events where one electron is misidentified as a photon ($WZ(\rightarrow \ell\ell\ell\nu)$, and $ZZ(\rightarrow \ell\ell\ell\ell)$), are estimated directly from MC.

6.1 Z + jets background

A two-dimensional sideband method [59] similar to the one in Ref. [18] is used to estimate the background in every distribution differentially. In addition to the SR and the $t\bar{t}\gamma$-CR, three additional Z + jets-CR are created to estimate this background by inverting either or both the isolation and the identification criteria on the photon. Photons that fail the *Tight* identification criteria must still satisfy a loose identification criteria, where the requirements on four EM calorimeter shower shape variables are removed, as described in Ref. [66]. Photon isolation is modified such that only the calorimeter-based component is considered, while track based isolation is applied in all regions. Photon candidates fail the isolation criteria when $E_{\mathrm{T}}^{\mathrm{iso}} > 0.065 \times E_{\mathrm{T}}^{\gamma} + E_{\mathrm{T}}^{\mathrm{gap}}$, where $E_{\mathrm{T}}^{\mathrm{gap}}$ is called energy gap. This gap is set to $E_{\mathrm{T}}^{\mathrm{gap}} = 2$ GeV and helps reduce the amount of $Z\gamma$ signal events leaking into the Z + jets-CRs (signal leakage).

The Z + jets-CRs described above are dominated by Z + jets events. The leakage of signal events into the Z + jets-CRs is removed via the signal leakage fractions estimated using the MC simulation of the signal. Backgrounds from other processes are subtracted using the MC simulation of each process. The yields of Z + jets events in the SR can then be derived from the number of events in the SR and in the three Z + jets-CRs, using the formulas described in Ref. [59].

Possible correlations between the isolation and the identification variables are estimated with Z + jets MC samples (PowhegBox) with the use of the correlation factor, R, that is the ratio between the fraction of Z + jets events satisfying the photon isolation requirement $E_{\mathrm{T}}^{\mathrm{iso}} < 0.065 \times E_{\mathrm{T}}^{\gamma}$ in events passing the identification criteria, over those that fail the identification criteria. In absence of correlation, this ratio would be equal to 1. While the sideband method is estimated in each bin of each differential distribution, the correlation is computed in larger intervals, or integrated, depending on the observable. This is done to preserve dependencies of the correlation where possible, while at the same time reduce statistical uncertainties. Results of the Z + jets estimate with larger intervals for the correlation computation are

compatible within uncertainties to the results with finer binning, but with reduced systematic and statistical uncertainties.

The uncertainty in the correlation factor R is obtained by varying the definition of the Z + jets-CRs both in data and MC; the $E_{\mathrm{T}}^{\mathrm{gap}}$ requirement is varied by ±1 GeV up and down and different loose identification criteria are used, for which three and five EM calorimeter shower shape variables are removed from the *Tight* criteria instead of four. In the inclusive phase-space, the correlation factor is estimated to be $R = 1.30 \pm 0.04$ (stat.) $\pm$ 0.23 (syst.). A cross-check of this estimation is performed by computing R in a Z + jets-CR where photons also fail the track isolation, and is estimated to be $R = 1.29 \pm 0.02$ (stat.), in agreement with the nominal estimation. Another source of uncertainty arises from the estimation of the $Z\gamma$ signal leakage into the Z + jets-CRs. The signal leakage factors are computed using Sherpa 2.2.11 and found to be small; the uncertainty is estimated by using `MadGraph` instead of Sherpa. Additional sources of uncertainties on R arise from the subtraction of other backgrounds (such as diboson events, or $t\bar{t}\gamma$). For these, the uncertainties in the cross sections are propagated to the final Z + jets estimate. The total uncertainty (including statistical uncertainties) in the integrated Z + jets estimate is then 22% and is dominated by the uncertainty of the data-driven method.

6.2 Pile-up background

Selected photons may originate from different pp collisions in the same bunch crossing because photons do not have requirements on the longitudinal position with respect to the primary vertex (z_γ), which is not a well-measured quantity. The reconstructed photon z_γ is determined by using a weighted mean of the intersections of the direction obtained from the electromagnetic cluster by taking into account the longitudinal segmentation of the calorimeter, with a constraint from the beam spot position and a typical resolution of 15 mm.

This background is estimated with a method similar to the one described in Ref. [18], by evaluating the fraction of pile-up events in data (f_{PU}), and it is briefly described here. To select photons with a better resolution $\sigma(z_\gamma)$, only photons that converted to electron-positron pairs with two tracks in the pixel detector are considered. Additionally, the radial conversion position of the photons must be between 5 mm from the beam spot (outside the beam pipe) and 125 mm (before the end of the pixel detector). The f_{PU} of converted photons is assumed to be the same as unconverted ones. This assumption is checked using a sample of signal MC events; in this sample, the fraction of events with truth-matched photons is the same for events with and without photon conversion. This is expected since the two effects (i.e. pile-up fraction and convertion fraction) should not be correlated.

The distribution of the primary vertex position z_{vtx} is a Gaussian distribution measured to have a width of $\sigma(z_{vtx}) \sim 35$ mm [18], corresponding to the width of the luminous region. The fraction of PU events (f_{PU}) can then be written as:

$$f_{PU} = \frac{1}{N_{\text{Data, pixel conv}}} \cdot \frac{N^{|\Delta z|>50\,\text{mm}}_{\text{Data, pixel conv}} - N^{|\Delta z|>50\,\text{mm}}_{Z\gamma\text{MC, pixel conv}}}{P(\Delta z > 50\ \text{mm})}, \tag{1}$$

where $N^{|\Delta z|>50\,\text{mm}}_{PU,\,\text{pixel conv}}$ is the number of pile-up events in a pile-up dominated region, defined as the region with $|\Delta z| > 50$ mm, with $|z_{vtx} - z_\gamma| = |\Delta z|$. Since the pile-up events are distributed as a Gaussian with width $\sigma(z_{vtx} - z_\gamma) = \sqrt{2}\sigma(z_{vtx}) \sim 50$ mm, the probability of observing events with $|\Delta z| > 50\,\text{mm}$ is estimated as $P(|\Delta z| > 50\,\text{mm}) = 0.32$. The term $N_{Z\gamma\text{MC, pixel conv}}$ describes the MC events where the Z

boson and the photon come from the same pp collision, and is taken from $Z\gamma$ MC. The MC is normalized to the data at $|\Delta z| < 5$ mm. The $|z_{vtx} - z_\gamma|$ distribution is showed in Fig. 3 of Ref. [18].

To have a better description of the pile-up events in the differential observables, f_{PU} is computed as a function of N_{Jet} and p_{T}^{γ}, f_{PU} varies from 0.02 to 0.08.

The procedure described above gives the total fraction of pile-up events in bins of p_{T}^{γ} and N_{Jet}, while the shape information for the other differential distributions is taken from MC events at particle level. A sample is built by adding together a generated single photon sample and a generated Z + jets sample. Only jets from the Z + jets sample are considered, since in data and in reconstructed MC, the jets are required to be associated to the vertex with the highest $\sum p_{\text{T}}^2$ of associated tracks through the JVT requirement, which is likely to reject the jets produced in association of the photon.

The difference between the nominal particle level sample and a pile-up enriched sample is assigned as an uncertainty. This additional pile-up enriched sample is selected from the data, by selecting only events where z_γ is closer to the vertex with the second highest $\sum p_{\text{T}}^2$ of associated tracks than the primary one. By definition, these events will be pile-up-like events. In observables that depend on jets, the difference between this particle level distribution and the one obtained considering all the jets is added as an additional uncertainty.

6.3 Other backgrounds

Background contributions from $t\bar{t}\gamma$, triboson ($WW\gamma/WZ\gamma$) events and diboson events, where one lepton is misidentified as a photon ($WZ \to \ell\ell\ell\nu$), are estimated with simulated samples. The most important of these is the $t\bar{t}\gamma$ process, which is around four times larger than the others, and therefore its modelling is checked in a dedicated CR. The CR is selected by requiring an electron-muon pair with opposite-sign and a photon. All other selection criteria from the SR are applied. The $t\bar{t}\gamma$ sample is scaled by a normalization factor of 1.44 and a relative uncertainty of 15% is assigned to this normalization [67].

Fig. 2 shows the comparison between data and MC in the $t\bar{t}\gamma$ CR for N_{Jet} and $p_{\text{T}}^{\gamma}/\sqrt{H_{\text{T}}}$. The fake photon estimate is obtained using the same method as previously described for the Z + jets background, but using $e\mu\gamma$ events instead of $ee\gamma/\mu\mu\gamma$ events. The correlation factor is fixed to $R = 1.30 \pm 0.04$ (see Sec. 6.1), where the uncertainty is only statistical. Another background also present in this region is from diboson events where one lepton is misidentified as a photon ($WZ \to \ell\ell\ell\nu$). The uncertainty on these background is set to 30%. Good agreement is seen between data and MC in the $t\bar{t}\gamma$ CR. The largest discrepancy can be seen in the 0-jet bin. This difference is due to mismodeling of the $t\bar{t}\gamma$ sample (the simulation is only at leading order) at low jet multiplicity, or triboson processes such as $WW\gamma$ or $WZ\gamma$, that are yet to be observed, or additional missing processes. Such mismodelling has negligible impact on the analysis since the contribution of $t\bar{t}\gamma$ and diboson processes for events with no jets in the SR is more than one order of magnitude smaller compared to the signal.

The other backgrounds (tribosons and dibosons) contribute around 1% of the total expected yield in the SR. For this reason they are estimated directly from MC. Other even smaller backgrounds (such as $H \to Z\gamma$) are neglected, since they contribute to less than 0.03% events in total.

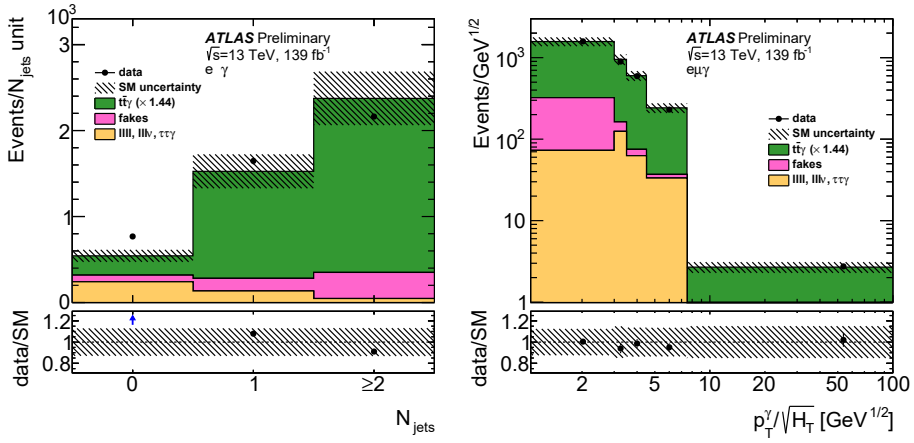

(a) (b)

Figure 2: Data (black dots) in the $t\bar{t}\gamma$ CR compared to scaled simulated $t\bar{t}\gamma$ events, simulated diboson events and fake photons estimated with a side-band method. The bottom panel shows the ratio of observed data events to the sum of the estimates. The signal and background distributions are stacked to produce the figures. The hatched band represents the statistical and the systematic uncertainties on the SM MC background yields added in quadrature.

6.4 Data event yield, signal, and background estimates comparisons in the signal region

Table 3 shows the data event yield and the signal and background estimates in the SR. SHERPA 2.2.11 MC is used for the $Z\gamma$ process. The statistical and systematic (see Section 8) uncertainties are also included in the Table.

Source	ee + $\mu\mu$	
$Z\gamma$+jets signal	73 500	±50 (stat.) ± 2 600 (syst.)
Z + jets	9 800	±460 (stat.) ± 2 100 (syst.)
$t\bar{t}\gamma$	3 600	±10 (stat.) ± 540 (syst.)
pile-up	2 500	±70 (stat.) ± 700 (syst.)
multiboson	950	±5 (stat.) ± 160 (syst.)
$tW\gamma$	150	±1 (stat.) ± 45 (syst.)
Total prediction	90 500	±500 (stat.) ± 3 500 (syst.)
Data	96 410	

Table 3: Data yield and the signal and background estimates in the SR. The systematic uncertainty includes only experimental uncertainties.

Figs. 3 and 4 show the comparison between the data and the expected SM events in a subset of distributions. The SHERPA 2.2.11 signal sample is scaled by a normalization factor of 1.08 to match the data. The normalization factor is obtained from the ratio of the measured yields to the predicted yields from SHERPA NLO, as shown in Table 3.

A general good agreement is observed between the data and the SM estimates. Observables inclusive in the number of jets are well modelled, while a small underestimation is observed at high $p_{\mathrm{T}}^{\ell\ell\gamma\mathrm{j}}$ and m_{jj}. However these are covered by the theory uncertainties of the signal, which are not included in the error bands in this figure, and range between 5% to 20% depending on the phase-space.

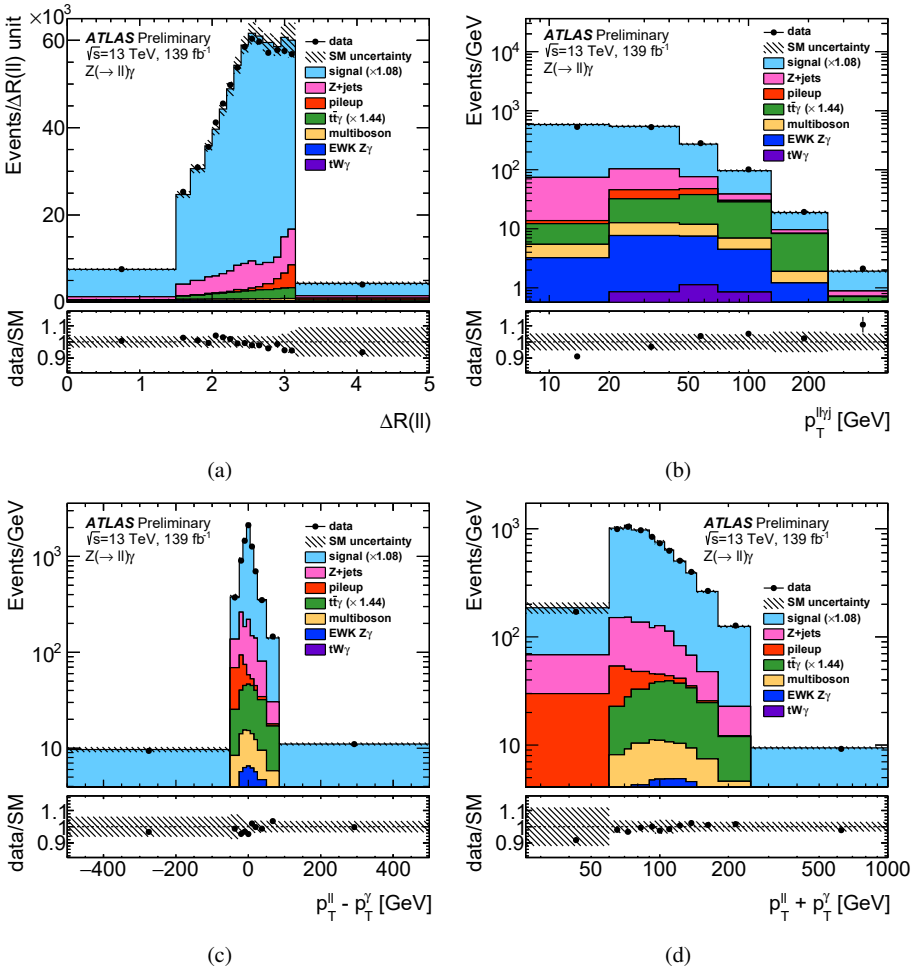

Figure 3: The measured (*a*) $\Delta R(\ell,\ell)$, (*b*) $p_{\mathrm{T}}^{\ell\ell\gamma\mathrm{j}}$, (*c*) $p_{\mathrm{T}}^{\ell\ell} - p_{\mathrm{T}}^{\gamma}$, and (*d*) $p_{\mathrm{T}}^{\ell\ell} + p_{\mathrm{T}}^{\gamma}$ distribution (dots) in the signal region. The error bars represent the data statistical uncertainty; for most of the points, the error bars are smaller than the marker size and, thus, not visible. The MC simulation of the signal from SHERPA 2.2.11 (blue histograms) and various backgrounds are also included. The signal and background distributions are stacked to produce the figures. The lower part of each figure shows the ratio of the data and the total SM distribution. The hatched band represents the statistical and the systematic uncertainties on the SM MC background yields added in quadrature, excluding theory uncertainties on the signal.

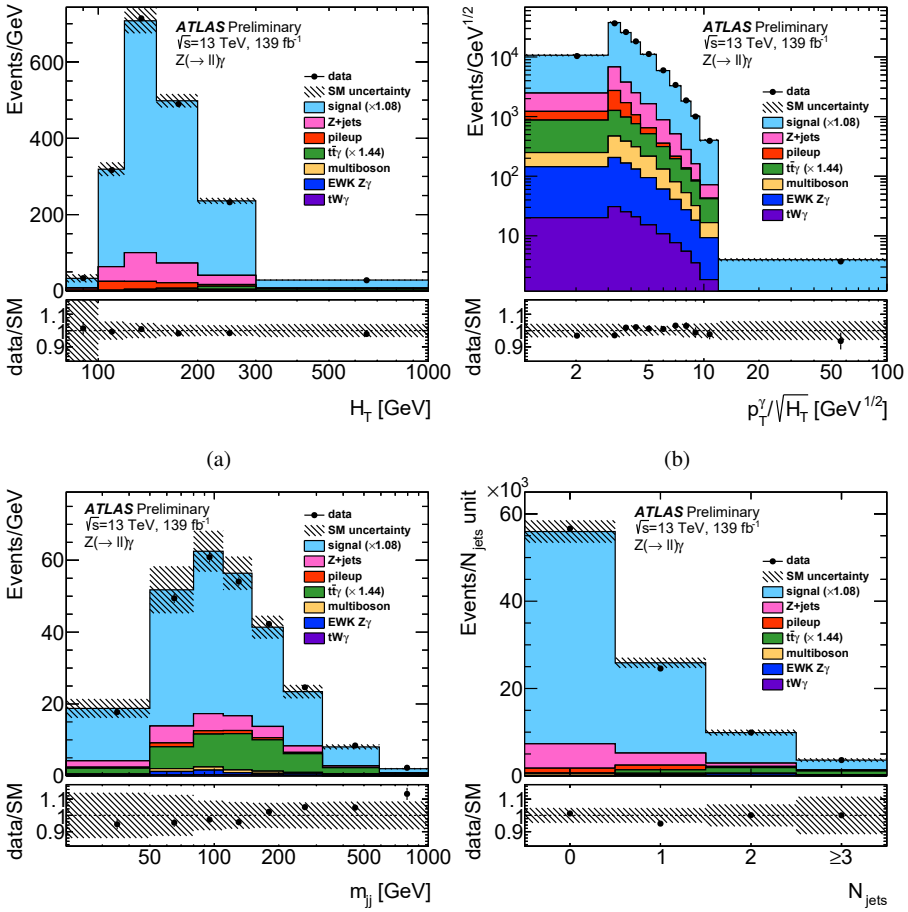

Figure 4: The measured (*a*) H_{T}, (*b*) $p_{\mathrm{T}}^{\gamma}/\sqrt{H_{\mathrm{T}}}$, (*c*) m_{jj}, and (*d*) N_{Jet} distribution (dots) in the signal region. The error bars represent the data statistical uncertainty; for most of the points, the error bars are smaller than the marker size and, thus, not visible. The MC simulation of the signal from SHERPA 2.2.11 (blue histograms) and various backgrounds are also included. The signal and background distributions are stacked to produce the figures. The lower part of each figure shows the ratio of the data and the total SM distribution. The hatched band represents the statistical and the systematic uncertainties on the SM MC background yields added in quadrature, excluding theory uncertainties on the signal.

7 Cross-Section determination

7.1 Fiducial region at particle level

The measurement are unfolded in a fiducial phase-space defined by particle level quantities. The fiducial phase-space in this analysis is built to be as close as possible to the detector-level selection discussed in Section 4, with selection criteria that minimise the extrapolation and allow comparisons with theoretical predictions. The phase-space is selected for $Z\gamma \to \ell^+\ell^-\gamma$ events, with ℓ being either an electron or muon. Only stable particles (with a mean lifetime $c\tau > 10$ mm) are used in the definition of the fiducial region. Additionally only "prompt" leptons (dressed) and photons are considered, i.e. only those that do not originate from hadron decays.

Leptons are required to pass the same p_{T} requirements as the SR: $p_{\mathrm{T}}(\ell_1) > 30$ GeV, $p_{\mathrm{T}}(\ell_2) > 25$ GeV. However the η requirements are different: for both electrons and muons $|\eta(\ell)| < 2.47$ is required, since at particle level the discontinuities in the detector are not present. A particle level isolation is applied to photons by requiring that the scalar sum of the E_{T} of all particles, except muons and neutrinos, within a cone of radius $R = 0.2$ around the photon has to be less than 7% of E_{T}^{γ}. This selection is the same as in Ref. [18] and is optimised trying to achieve the same level of acceptance in both detector-level and particle level selections. Similarly, photons are rejected if they are within a distance of $\Delta R = 0.4$ of any lepton. Jets are obtained by clustering stable particle excluding prompt leptons using the anti-k_t algorithm with a radius of $R = 0.4$. Photons associated around prompt leptons in a cone of $R = 0.1$ are also excluded. Jets are defined in the same way as for the SR, by requiring $p_{\mathrm{T}} > 30$ GeV for $|\eta| < 2.5$ and $p_{\mathrm{T}} > 50$ GeV for $2.5 < |\eta| < 4.5$. In the SR this selection is used to find a compromise between reducing pile-up jets and maintaining good statistics at low p_{T}. Jets are rejected if they are within a distance of $\Delta R = 0.4$ of any photon. As in the SR, $m_{\ell\ell} > 40$ GeV and $m_{\ell\ell} + m_{\ell\ell\gamma} > 182$ GeV. A pair of opposite-sign, same-flavour leptons is selected, and no additional veto on the number of leptons is required.
Table 4 summarises the fiducial selection used in the analysis.

Quantity	Selection criteria
lepton kinematics	$p_{\mathrm{T}}(\ell_1) > 30$ GeV, $p_{\mathrm{T}}(\ell_2) > 25$ GeV, $\|\eta\| < 2.47$
photon kinematics	$p_{\mathrm{T}}^{\gamma} > 30$ GeV, $\|\eta\| < 2.37$, $\Delta R(\gamma, \ell) > 0.4$
photon isolation	$E_{\mathrm{T}}^{cone20}/E_{\mathrm{T}}^{\gamma} < 0.07$
jet kinematics	($p_{\mathrm{T}} > 30$ GeV if $\|\eta\| < 2.5$) or ($p_{\mathrm{T}} > 50$ GeV if $2.5 < \|\eta\| < 4.5$), $\Delta R(\gamma, \mathrm{jet}) > 0.4$
invariant mass	$m_{\ell\ell} > 40$ GeV, $m_{\ell\ell} + m_{\ell\ell\gamma} > 182$ GeV

Table 4: Definition of the fiducial region at particle level.

7.2 Fiducial and differential cross section

The fiducial cross section is evaluated in the fiducial region described in the previous section. It is obtained with the following formula:

$$\sigma^{\mathrm{fid}} = \frac{N_{\mathrm{obs}} - N_{\mathrm{bkg}}}{C \times \mathcal{L}},$$

where N_{obs} and N_{bkg} are the observed number of events and the expected number of background events, respectively, $\mathcal{L}$ is the luminosity, and C is the correction factor which accounts for detector inefficiency and resolution effects. C is calculated as the number of simulated $Z\gamma$ events entering the detector-level SR divided by the number of simulated $Z\gamma$ events entering the fiducial volume. The inclusive C factor is obtained with SHERPA 2.2.11 MC, combining ee and $\mu\mu$ channels; its value is found to be $C = 0.543 \pm 0.001\,(\text{stat}) \pm 0.02\,(\text{syst})$.

Differential cross sections are evaluated in the fiducial signal region for several observables.

The event yields in the e^+e^- and in the $\mu^+\mu^-$ decay channels are added together and unfolded in a single step. The distributions are unfolded using an Iterative Bayesian Method [68], with two iterations as nominal values. $Z\gamma$ events simulated with SHERPA 2.2.11 are used to produce response matrices used to correct for the migration between bins in the detector-level and particle-level distributions. Additionally, the unfolding corrects for fiducial and reconstruction efficiencies. These are respectively the probability of having particle-level events pass the detector-level SR criteria, and the probability of detector-level events originating from outside the fiducial region.

8 Systematic uncertainties

Different sources of systematic uncertainties affect this measurement: experimental uncertainties due to detector reconstruction, uncertainties in the background estimate (both from simulated samples and data-driven methods, as described in section 6), systematic uncertainties in the unfolding, and theoretical uncertainties in the signal prediction.

Systematic uncertainties are propagated to the unfolded results by using a different set of inputs to the unfolding and migration matrix, obtained by varying the kinematics or event weights by 1 σ, and computing the difference with the nominal cross sections; this difference is taken as the systematic uncertainty.

Experimental uncertainties account for the finite resolution of the objects reconstructed by the ATLAS detector, their calibration, and the modelling of the reconstruction in the simulation. Uncertainties affecting the electrons and photons include the uncertainties in the energy scale and resolution [57], while for muons uncertainties are considered for the momentum resolution [69]. Both leptons and photons have uncertainties in the efficiency of the identification and the isolation [57, 69]. Uncertainties in the lepton trigger efficiencies are also considered [55, 56]. Jet uncertainties account for both the energy scale (JES) and the resolution (JER) [70]. JES uncertainties take into account detector modelling, statistical effects, flavour composition, and the description of pile-up jets. JVT efficiency uncertainties are also considered [64]. Additional uncertainties are added that take into account the modelling of the number of pp collisions (μ). An uncertainty of 1.7% in the total luminosity is considered in this analysis.

The statistical uncertainty in the unfolded distributions is evaluated using pseudo-data (toys). Input spectra and migration matrices are fluctuated using a Poisson distribution centered around the nominal value in each bin. These new inputs are then unfolded, and the root mean square (RMS) of the new distribution is used as uncertainty.

The unfolding procedure is based on the choice of an assumption, the simulated signal sample. This choice can bias the results, and a systematic uncertainty must be applied to account for it. This uncertainty is obtained through a data-driven closure test. The simulated signal distributions are reweighted with a smooth function obtained by requiring that the detector-level distribution matches the data (with the

N_{Jet}	0	1	2	> 2
Source	Uncertainty [%]			
Electrons	1.0	0.9	0.8	0.8
Muons	0.3	0.3	0.3	0.4
Jets	1.7	1.7	4.5	8.8
Photons	1.4	1.3	1.3	1.2
Pile-up	2.1	0.8	0.2	0.3
Background	1.8	1.8	3.0	4.4
Stat. MC	0.1	0.2	0.3	0.4
Stat. data	0.8	1.5	1.8	1.9
Luminosity	1.7	1.7	1.7	1.7
Theory	0.6	0.2	1.4	1.0
Total	4.2	3.8	6.3	10.3

Table 5: Impact of the different systematic uncertainties on the cross section as a function of N_{Jet} in each bin of the distribution.

background subtracted). The reweighted distribution is then unfolded, treating this sample as pseudo-data, and using the transfer matrix from the reweighted distributions. The uncertainty is obtained by comparing this result with the nominal unfolded result.

Uncertainties in the unfolding procedure due to the theoretical modelling are obtained by repeating the unfolding procedure with alternative signal simulations. Uncertainties in the signal predictions are due to missing higher order contributions in the cross section calculation, the uncertainties in the PDF choice, and the uncertainties in α_S. The scale variations are obtained by varying the renormalization (μ_R) and factorisation (μ_F) scale in the signal simulation by a factor of two up and down around their nominal values. Uncertainties are obtained by taking an envelope: in each bin the highest variation is kept as an uncertainty. Additional uncertainties are added to account for the choice of a specific PDF in the cross section calculation. Following the PDF4LHC recommendation [71], the NNPDF30_nnlo_as_0118 PDF set is used as nominal set, and is compared with results obtained with weights stored in the SHERPA samples. An envelope is then taken of all the variations. A similar approach is used for the α_s variations, where the NNPDF30_nnlo_as_0117 and NNPDF30_nnlo_as_0119 PDF sets are used. For theory predictions, uncertainties are obtained by taking an envelope of the difference between the nominal and the variations.

Uncertainties on the background estimates are taken to be 30% on the diboson cross section and 15% on $t\bar{t}\gamma$ cross section (which corresponds to the uncertainty of the normalization factor from the LO cross section to NLO cross section [48]). The uncertainty of 30% on the diboson cross section cover both the nominal uncertainty [72] and the typical size of the mismodeling of non-prompt objects. The systematic uncertainties for the Z + jets background are estimated as described in Section 6.1, and are propagated through the unfolding framework.

Table 5 shows the breakdown of the systematic uncertainties on the cross section as a function of N_{Jet}. The last row in the table is the total relative uncertainty obtained as the sum in quadrature of each systematic and statistical uncertainties.

9 Results

As presented in Ref. [18], the fiducial cross section is $\sigma = 533.7 \pm 2.1\,(\text{stat}) \pm 12.4\,(\text{syst}) \pm 9.1\,(\text{lumi})$ fb. The predicted fiducial cross sections from Sherpa 2.2.11 is 479.5 ± 0.3 (stat) fb and for MiNNLO$_{PS}$ is 493.0 ± 3.0 (stat).

Results are obtained by unfolding the $Z\gamma$ signal together with the electroweak production of $Z\gamma$.

Figs. 5 to 12 show the measured differential cross sections as functions of the different observables. The theoretical predictions from the calculations of Sherpa 2.2.4, Sherpa 2.2.11 and Madgraph, and from the NNLO predictions of MiNNLO$_{PS}$ and MATRIX are compared to the measurements in these figures. In general, Sherpa samples underestimate the total cross section, with the Sherpa 2.2.11 (NLO) being higher than Sherpa 2.2.4, while Madgraph, MiNNLO$_{PS}$ and MATRIX show general good agreement for the total cross section. Between the two Sherpa samples, 2.2.11 has a general better agreement also in the shapes, especially for the number of jets.

The Z-boson momentum is a fundamental observable, correlated with the jet activity, and its difference to p_{T}^{γ} is an observable that probes perturbative QCD over a wide range of scales, while $p_{\mathrm{T}}^{\ell\ell} + p_{\mathrm{T}}^{\gamma}$ describes the hard scale of the process. Fig. 5 shows the differential cross section as function of the observables $p_{\mathrm{T}}^{\ell\ell}$, $p_{\mathrm{T}}^{\ell\ell} - p_{\mathrm{T}}^{\gamma}$, $p_{\mathrm{T}}^{\ell\ell} + p_{\mathrm{T}}^{\gamma}$, and $\Delta R(\ell, \ell)$. All the generators show good agreement with the measurements, even if Sherpa generally underestimates the data. MATRIX calculations are also in good agreement.
Jet multiplicity is a fundamental observable to probe QCD and additional soft radiation [23]. The ratio $p_{\mathrm{T}}^{\mathrm{Jet2}}/p_{T}^{\mathrm{Jet1}}$ in particular is an observable that tests the limits of PS effects and resummation of Sudakov logarithms. Differential cross sections for jet observables are shown in Fig. 6. The differential cross section is dominated by events with zero jets, and rapidly falls off with increasing QCD emission. Leading and subleading jets are mostly produced with similar p_{T}; however, there are also a few events in which the leading jet has a significantly higher p_{T} than the subleading one. In general MC samples are in good agreement with the data, however at high jet multiplicity and high jet transverse momentum Sherpa 2.2.4 predicts higher yields than Sherpa 2.2.11, while Madgraph has lower yields than both in N_{Jet} but it is comparable to the Sherpa samples in the leading ($p_{\mathrm{T}}^{\mathrm{Jet1}}$) and subleading ($p_{\mathrm{T}}^{\mathrm{Jet2}}$) jet momentum. MiNNLO$_{PS}$ instead predicts softer jets and with less multiplicity, while MATRIX seems to model better the jet momentum spectrum, but predicts higher jet multiplicity. It is worth noting that MATRIX produces only up to 2 jets, therefore the last bin is empty for this calculation. The ratio $p_{\mathrm{T}}^{\mathrm{Jet2}}/p_{T}^{\mathrm{Jet1}}$ is equally well described by both Sherpa models and Madgraph. MATRIX is also in good agreement, while MiNNLO$_{PS}$ underestimates this distribution.

The invariant mass of the two leading jets is an important observable that describes the hard scale of the process and its precise modelling is fundamental for the $Z\gamma$ QCD background in searches for the electroweak $Z\gamma$ production or new physics [73]. The m_{jj} distribution in Fig. 7 is well modelled in general, except for MiNNLO$_{PS}$ that underestimates the highest bins. MATRIX shows a few bins with some overestimations between 60 and 100 GeV, that are due to statistical fluctuations in the predictions. The invariant mass $m_{\ell\ell\gamma j}$ is a variable sensitive to the hard scale of the process, and is also well modelled by MC generators, except the last bins for MiNNLO$_{PS}$, where an underestimation is shown. MATRIX also shows good agreement, with a small overestimation (within uncertainty) in the last bins.

Fig. 8 shows additional jet observables H_{T}, $p_{\mathrm{T}}^{\gamma}/\sqrt{H_{\mathrm{T}}}$, $\Delta\phi(\mathrm{Jet}, \gamma)$, and $p_{\mathrm{T}}^{\ell\ell\gamma\mathrm{j}}$. H_{T} and $p_{\mathrm{T}}^{\gamma}/\sqrt{H_{\mathrm{T}}}$ are both well described by both Sherpa 2.2.4 and Sherpa 2.2.11, while Madgraph, MATRIX, and MiNNLO$_{PS}$ underestimate the last bin of H_{T}. The $\Delta\phi(\mathrm{Jet}, \gamma)$ distribution is important for PS corrections in QCD

predictions in phase-space with soft QCD emission [23]. The measurement shows a preference for events where the photon and the leading jet are back-to-back. $\Delta\phi(\text{Jet},\gamma)$ is well modelled by all the predictions, except in the very first bin for MATRIX. The transverse momentum $p_{\text{T}}^{\ell\ell\gamma\text{j}}$ is well modelled within uncertainty by both SHERPA samples and Madgraph. Instead MiNNLO$_{PS}$ and MATRIX show steeper $p_{\text{T}}^{\ell\ell\gamma\text{j}}$ distributions.

Fig. 9 shows angular variables like $\cos\theta_{CS}$ and ϕ_{CS}, that are sensitive to the polarisation of the Z boson. The variation of $\cos\theta_{CS}$ with $p_{\text{T}}^{\ell\ell}$ is mainly due to the lepton selection which translates into differences in acceptance in each $p_{\text{T}}^{\ell\ell}$ region. For these variables SHERPA, Madgraph and MiNNLO$_{PS}$ are in general in good agreement for the shapes, even if, as already mentioned, SHERPA 2.2.4 and 2.2.11 generally underestimate the data. MATRIX calculations show some small discrepancy in $\cos\theta_{CS}$ in the very first $p_{\text{T}}^{\ell\ell}$ bin, but otherwise show very good agreement.

The ratio $p_{\text{T}}^{\ell\ell\gamma}/m_{\ell\ell\gamma}$ as a resolution variable is important to probe the effects of Sudakov logarithm terms in different regimes of hard scale of the process. The ratio $p_{\text{T}}^{\ell\ell\gamma}/m_{\ell\ell\gamma}$ in all the $m_{\ell\ell\gamma}$ slices is presented in Fig. 10. These observables are better modelled in SHERPA 2.2.11 than in SHERPA 2.2.4. MiNNLO$_{PS}$ shows a good agreement in all the $m_{\ell\ell\gamma}$ slices, while instead MATRIX overestimates the lowest bin in $p_{\text{T}}^{\ell\ell\gamma}/m_{\ell\ell\gamma}$.

The $p_{\text{T}}^{\ell\ell} - p_{\text{T}}^{\gamma}$ and $p_{\text{T}}^{\ell\ell\gamma\text{j}}$ distributions offer an important probe of additional soft QCD emissions, in increasing hard scale of the process $p_{\text{T}}^{\ell\ell} + p_{\text{T}}^{\gamma}$ and $p_{\text{T}}^{\ell\ell\gamma}$ respectively. The $p_{\text{T}}^{\ell\ell} - p_{\text{T}}^{\gamma}$ distributions become more asymmetric in regimes with harder scale of the process. All the different distributions of $p_{\text{T}}^{\ell\ell} - p_{\text{T}}^{\gamma}$ in slices of $p_{\text{T}}^{\ell\ell} + p_{\text{T}}^{\gamma}$ (Fig. 11) are well modelled by all the MC and MATRIX, except the last two bins in the slice with $p_{\text{T}}^{\ell\ell} + p_{\text{T}}^{\gamma} > 300$ GeV where Madgraph slightly overestimates the data. $p_{\text{T}}^{\ell\ell\gamma\text{j}}$ in slices of $p_{\text{T}}^{\ell\ell\gamma}$ (Fig. 12) is well modelled SHERPA and Madgraph, while MiNNLO$_{PS}$ underestimate the data for $p_{\text{T}}^{\ell\ell\gamma} > 75$ GeV. MATRIX exhibits softer spectrum than the other predictions in general.

In summary, SHERPA and Madgraph samples generally describe the data well, especially observables with jets, even if SHERPA underestimates the total cross section. MiNNLO$_{PS}$ and MATRIX calculations predict accurate descriptions of the observables especially in the inclusive case, but with some discrepancy at high jet multiplicity.

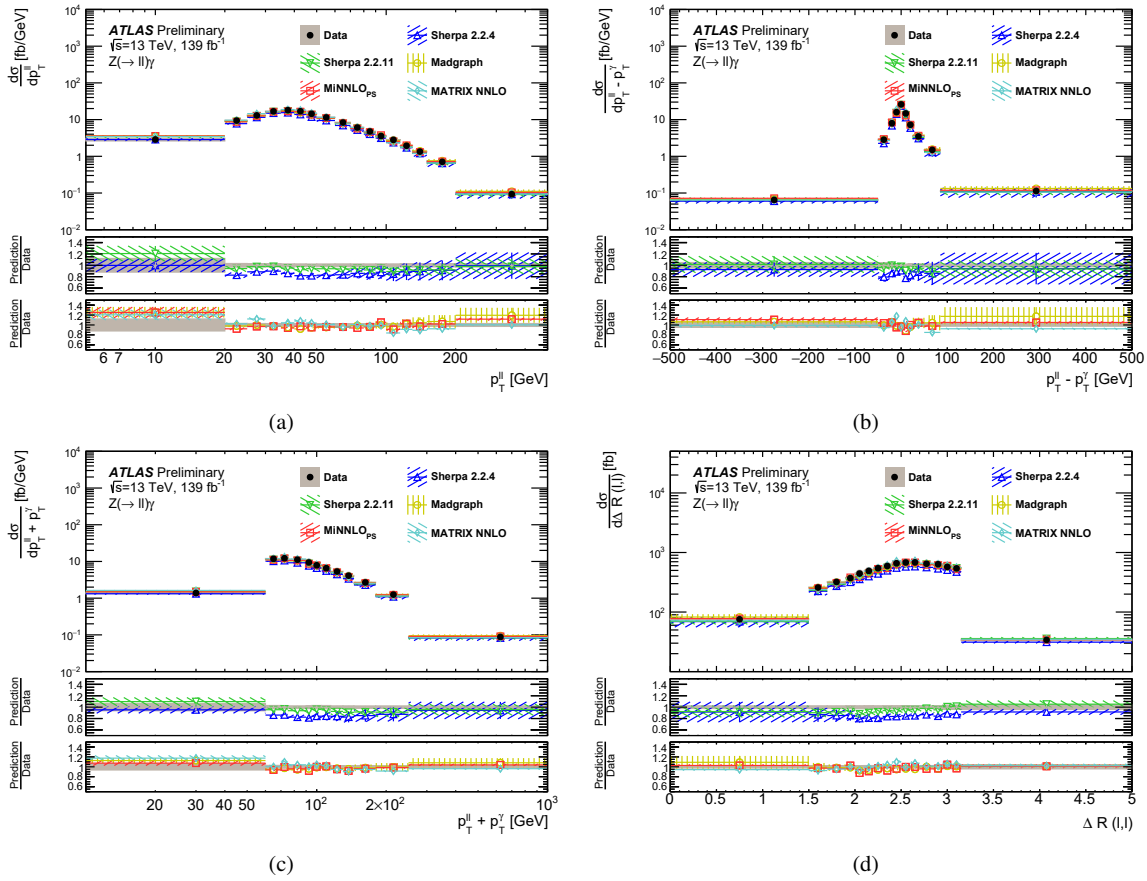

Figure 5: Measured differential cross section (black data points) as a function of observables (*a*) $p_{\mathrm{T}}^{\ell\ell}$, (*b*) $p_{\mathrm{T}}^{\ell\ell} - p_{\mathrm{T}}^{\gamma}$, (*c*) $p_{\mathrm{T}}^{\ell\ell} + p_{\mathrm{T}}^{\gamma}$, and (*d*) $\Delta R(\ell, \ell)$. Error bands on the data points show the statistical uncertainty, while the grey area shows the total uncertainty in the unfolded result. Measured cross sections are compared with SM predictions from event generators at particle level SHERPA 2.2.4, SHERPA 2.2.11, MadGraph5_aMCNLO, and MiNNLO$_{PS}$. Fixed order calculations results using MATRIX NNLO are also shown. Dashed bands represent statistical uncertainty and theoretical uncertainty (PDF and Scale variations). The bottom panels show the ratio of the SM prediction to the measured cross section.

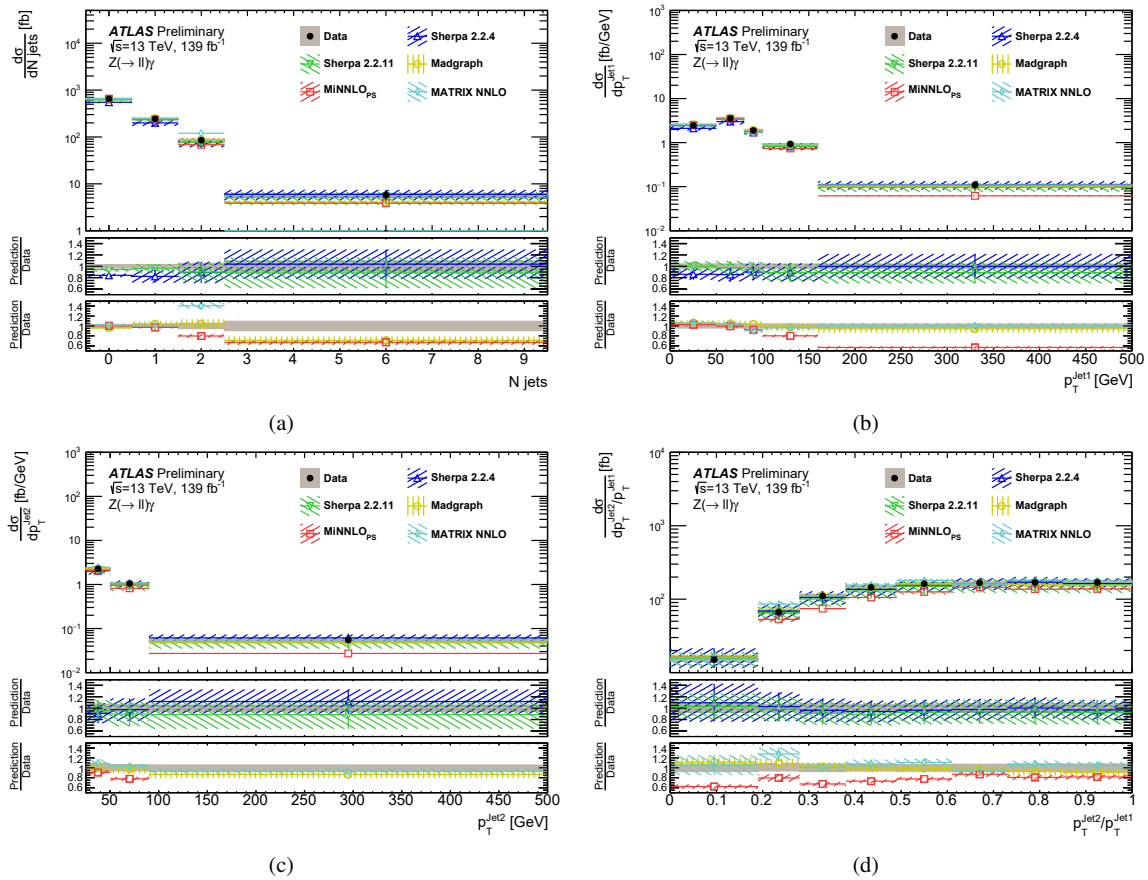

(a) (b) (c) (d)

Figure 6: Measured differential cross section (black data points) as a function of observables (*a*) N_{Jet}, (*b*) $p_{\text{T}}^{\text{Jet1}}$, (*c*) $p_{\text{T}}^{\text{Jet2}}$, (*d*) $p_{\text{T}}^{\text{Jet2}}/p_{T}^{\text{Jet1}}$. Error bands on the data points show the statistical uncertainty, while the grey area shows the total uncertainty in the unfolded result. Measured cross sections are compared with SM predictions from event generators at particle level SHERPA 2.2.4, SHERPA 2.2.11, MadGraph5_aMCNLO, and MiNNLO$_{PS}$. Fixed order calculations results using MATRIX NNLO are also shown. Dashed bands represent statistical uncertainty and theoretical uncertainty (PDF and Scale variations). The bottom panels show the ratio of the SM prediction to the measured cross section.

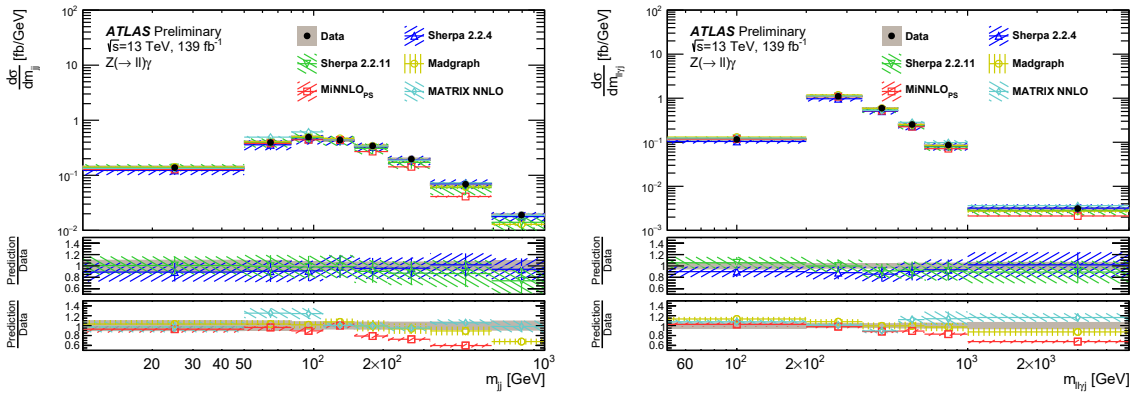

(a) (b)

Figure 7: Measured differential cross section (black data points) as a function of observables (*a*) m_{jj}, (*b*) $m_{\ell\ell\gamma j}$. Error bands on the data points show the statistical uncertainty, while the grey area shows the total uncertainty in the unfolded result. Measured cross sections are compared with SM predictions from event generators at particle level SHERPA 2.2.4, SHERPA 2.2.11, MadGraph5_aMCNLO, and MiNNLO$_{PS}$. Fixed order calculations results using MATRIX NNLO are also shown. Dashed bands represent statistical uncertainty and theoretical uncertainty (PDF and Scale variations). The bottom panels show the ratio of the SM prediction to the measured cross section.

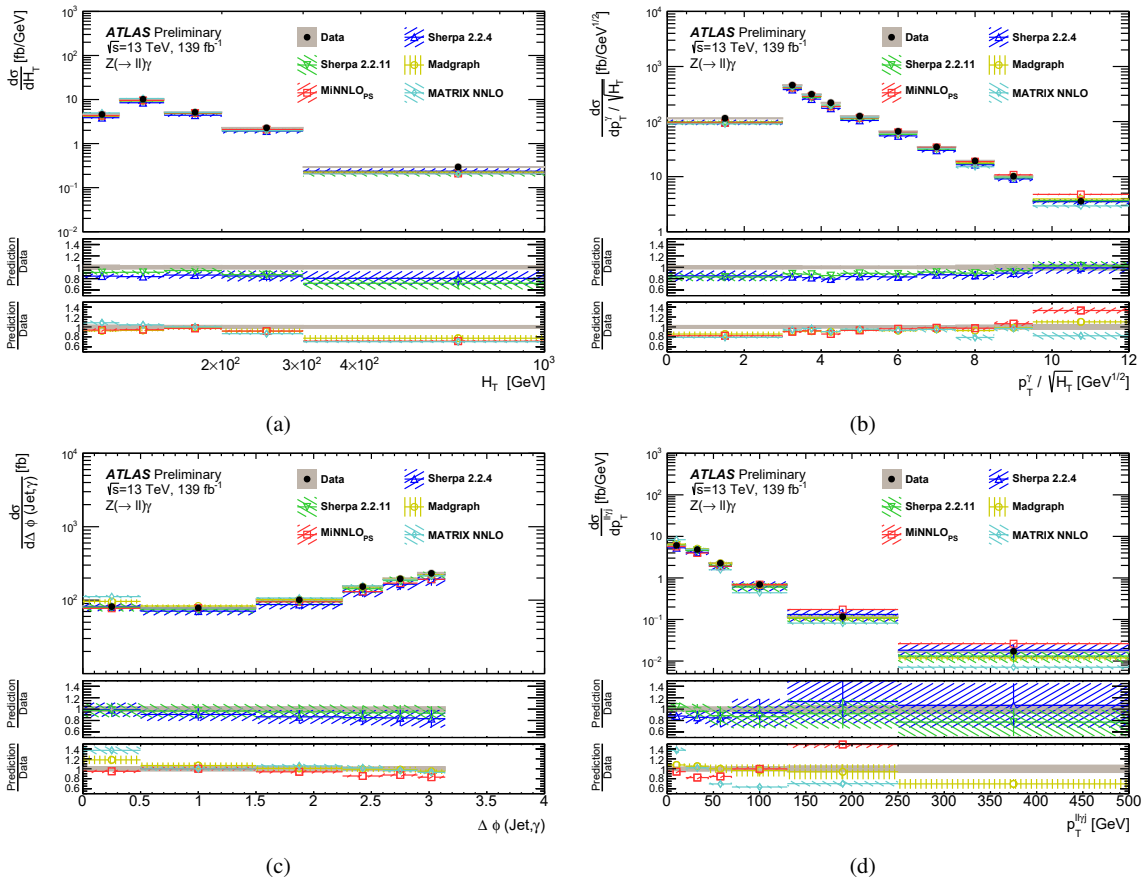

Figure 8: Measured differential cross section (black data points) as a function of observables (*a*) H_{T}, (*b*) $p_{\mathrm{T}}^{\gamma}/\sqrt{H_{\mathrm{T}}}$, (*c*) $\Delta\phi(\mathrm{Jet},\gamma)$, (*d*) $p_{\mathrm{T}}^{\ell\ell\gamma\mathrm{j}}$. Error bands on the data points show the statistical uncertainty, while the grey area shows the total uncertainty in the unfolded result. Measured cross sections are compared with SM predictions from event generators at particle level SHERPA 2.2.4, SHERPA 2.2.11, MadGraph5_aMCNLO, and MiNNLO$_{PS}$. Fixed order calculations results using MATRIX NNLO are also shown. Dashed bands represent statistical uncertainty and theoretical uncertainty (PDF and Scale variations). The bottom panels show the ratio of the SM prediction to the measured cross section.

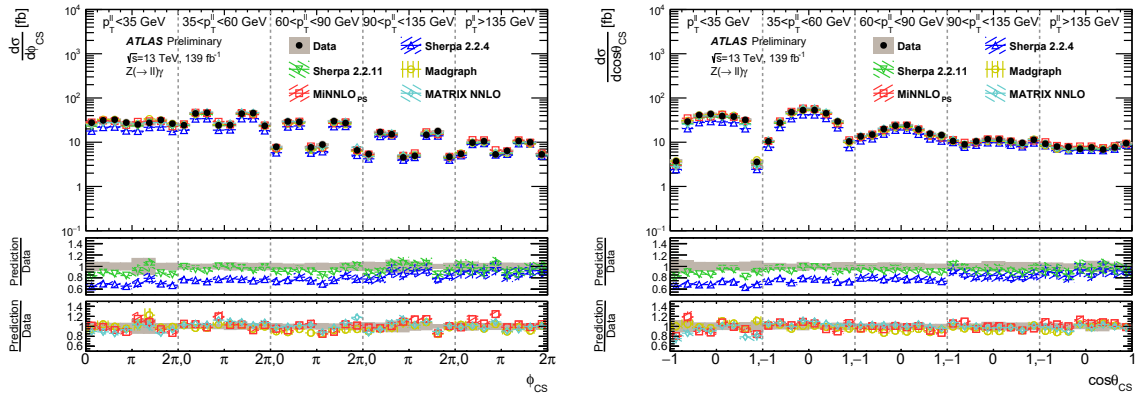

(a) (b)

Figure 9: Measured differential cross section (black data points) as a function of the observables (*a*) ϕ_{CS} and (*b*) $\cos\theta_{CS}$, in different bins of $p_{\mathrm{T}}^{\ell\ell}$. Error bands on the data points show the statistical uncertainty, while the grey area shows the total uncertainty in the unfolded result. Measured cross sections are compared with SM predictions from event generators at particle level SHERPA 2.2.4, SHERPA 2.2.11, MadGraph5_aMCNLO, and MiNNLO$_{PS}$. Fixed order calculations results using MATRIX NNLO are also shown. Dashed bands represent statistical uncertainty and theoretical uncertainty (PDF and Scale variations). The bottom panels show the ratio of the SM prediction to the measured cross section.

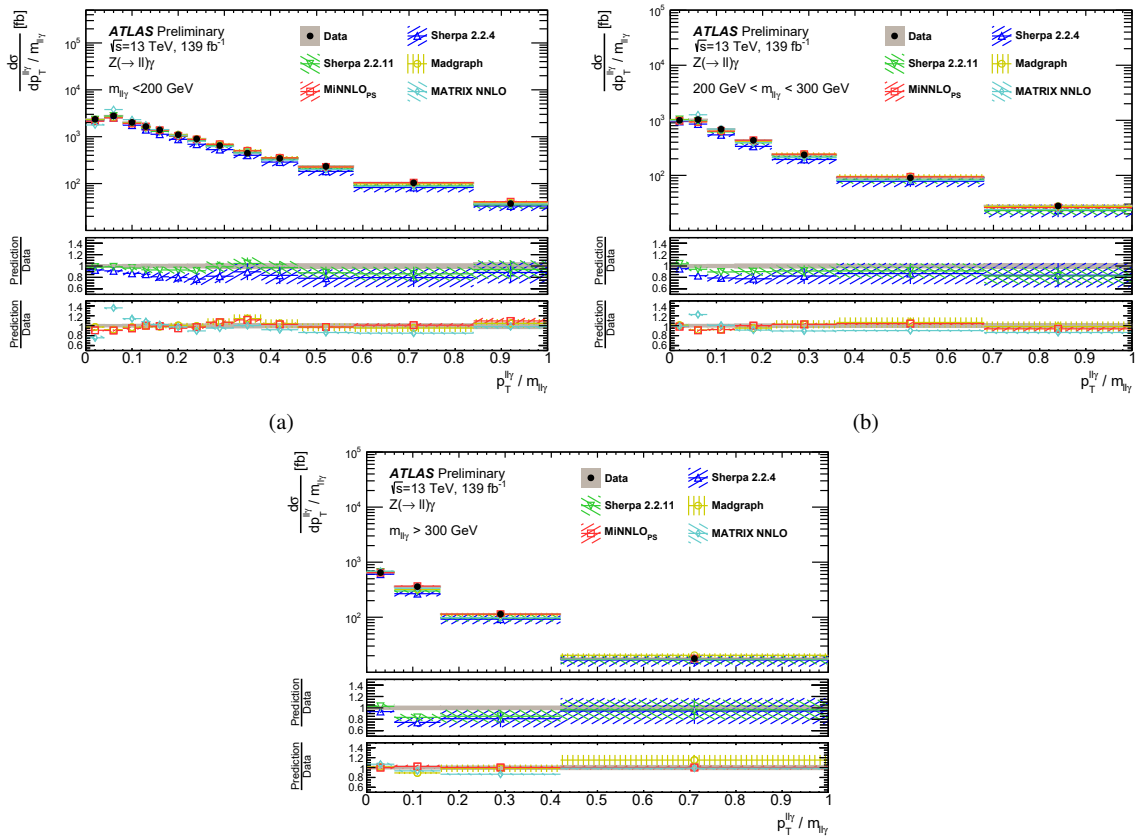

(a) (b)

(c)

Figure 10: Measured differential cross section (black data points) as a function of the $p_{\mathrm{T}}^{\ell\ell\gamma}/m_{\ell\ell\gamma}$ (a) in $m_{\ell\ell\gamma} < 200\,\mathrm{GeV}$, (b) in 200 GeV $< m_{\ell\ell\gamma} <$ 300 GeV, (c) in $m_{\ell\ell\gamma} > 300$ GeV. Error bands on the data points show the statistical uncertainty, while the grey area shows the total uncertainty in the unfolded result. Measured cross sections are compared with SM predictions from event generators at particle level Sherpa 2.2.4, Sherpa 2.2.11, MadGraph5_aMCNLO, and MiNNLO$_{PS}$. Fixed order calculations results using MATRIX NNLO are also shown. Dashed bands represent statistical uncertainty and theoretical uncertainty (PDF and Scale variations). The bottom panels show the ratio of the SM prediction to the measured cross section.

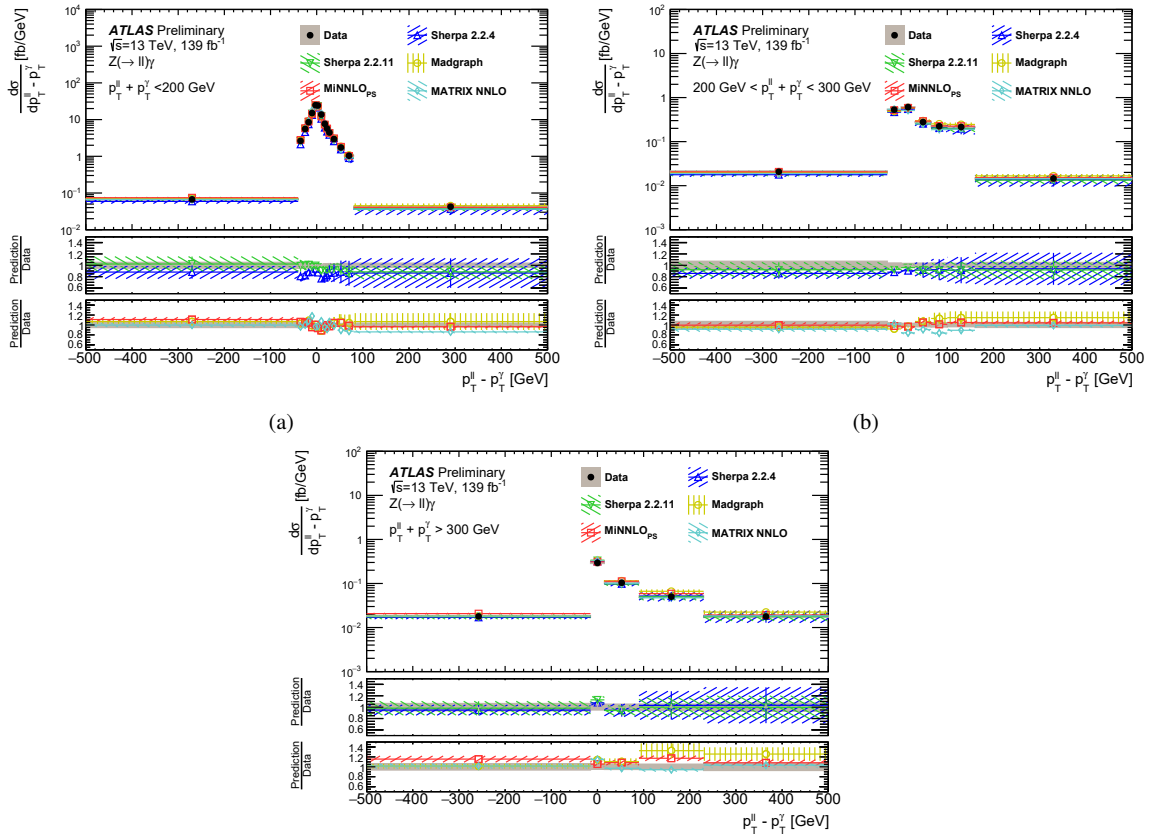

(a) (b)

(c)

Figure 11: Measured differential cross section (black data points) as a function of the $p_{\mathrm{T}}^{\ell\ell} - p_{\mathrm{T}}^{\gamma}$ (*a*) in $p_{\mathrm{T}}^{\ell\ell} + p_{\mathrm{T}}^{\gamma} < 200$ GeV, (*b*) in 200 GeV $< p_{\mathrm{T}}^{\ell\ell} + p_{\mathrm{T}}^{\gamma} < 300$ GeV, (*c*) in $p_{\mathrm{T}}^{\ell\ell} + p_{\mathrm{T}}^{\gamma} > 300$ GeV. Error bands on the data points show the statistical uncertainty, while the grey area shows the total uncertainty in the unfolded result. Measured cross sections are compared with SM predictions from event generators at particle level SHERPA 2.2.4, SHERPA 2.2.11, MadGraph5_aMCNLO, and MiNNLO$_{PS}$. Fixed order calculations results using MATRIX NNLO are also shown. Dashed bands represent statistical uncertainty and theoretical uncertainty (PDF and Scale variations). The bottom panels show the ratio of the SM prediction to the measured cross section.

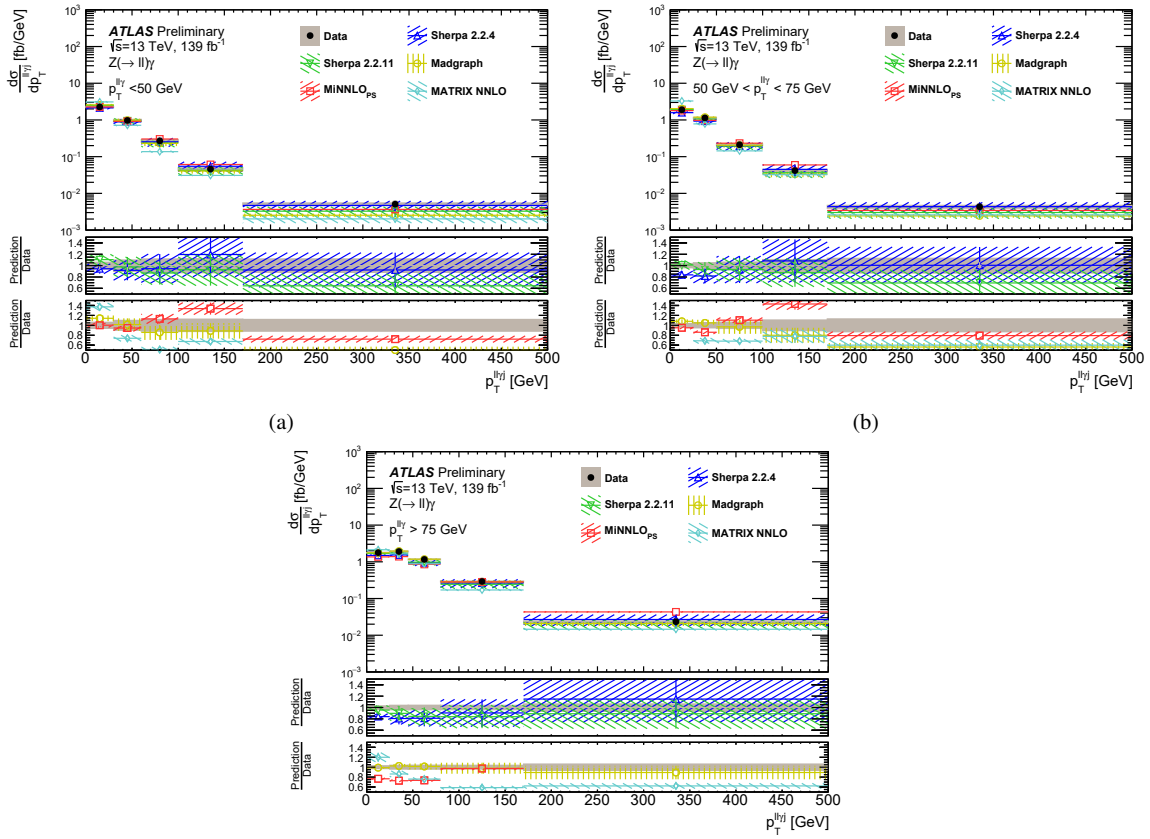

(a) (b)

(c)

Figure 12: Measured differential cross section (black data points) as a function of $p_{\mathrm{T}}^{\ell\ell\gamma\mathrm{j}}$ (a) in $p_{\mathrm{T}}^{\ell\ell\gamma} < 50$ GeV, (b) in 50 GeV $< p_{\mathrm{T}}^{\ell\ell\gamma} < 75$ GeV, (c) in 75 GeV $< p_{\mathrm{T}}^{\ell\ell\gamma}$. Error bands on the data points show the statistical uncertainty, while the grey area shows the total uncertainty in the unfolded result. Measured cross sections are compared with SM predictions from event generators at particle level Sherpa 2.2.4, Sherpa 2.2.11, MadGraph5_aMCNLO, and MiNNLO$_{PS}$. Fixed order calculations results using MATRIX NNLO are also shown. Dashed bands represent statistical uncertainty and theoretical uncertainty (PDF and Scale variations). The bottom panels show the ratio of the SM prediction to the measured cross section.

10 Conclusion

A measurement of several differential distributions for $Z\gamma$ production in association with jets is presented in this work, in the final state where the Z boson decays in two opposite-sign same-flavour leptons (e^+e^- or $\mu^+\mu^-$). The measurement is performed in a fiducial phase-space enhanced in ISR photons, where the sum of the invariant mass of the leptons and the invariant mass of the leptons and the photon are greater than twice the mass of the Z boson. The measurement is performed using data collected by the ATLAS detector from LHC pp collisions at $\sqrt{s} = 13$ TeV, using a total integrated luminosity of 139 fb^{-1}.

Differential cross sections are measured as a functions of the kinematics of jets, leptons, and photons. Both one-dimensional and two-dimensional distributions have been chosen that enhance the hard scatter effects from soft, collinear radiations. This result represents a precise measurement of $Z\gamma$ production in association with jets, with a total uncertainty between 4% and 10% depending on the number of jets. The results are compared to MC generators involving different precision of multileg merging at LO and NLO, as well as recent predictions at NNLO, including MiNNLO$_{\text{PS}}$, and fixed order calculations such as MATRIX. Measurements are in general in good agreement with the predictions. Jet activity is generally well described, however some trends are observed in the different generators. Variables that are sensitive to polarisation effects of the Z boson are well modelled by all MC generators, and by the MATRIX software.

The measurements of $Z\gamma$ production in association with jets have the potential to constrain the QCD predictions and improve resummation calculations in regions where Sudakov logarithm terms dominate.

References

[1] O. S. Brüning et al., eds., *LHC Design Report. Vol. I: The LHC Main Ring*, CERN-2004-003-V-1, CERN-2004-003, 2004, URL: https://cdsweb.cern.ch/record/782076 (cit. on p. 2).

[2] O. S. Brüning et al., eds., *LHC Design Report. Vol. II: The LHC infrastructure and general*, CERN-2004-003-V-2, CERN-2004-003, 2004, URL: https://cdsweb.cern.ch/record/782076 (cit. on p. 2).

[3] R. D. Ball et al., *Parton distributions from high-precision collider data*, Eur. Phys. J. C **77** (2017), ISSN: 1434-6052, URL: http://dx.doi.org/10.1140/epjc/s10052-017-5199-5 (cit. on p. 2).

[4] S. Alioli, C. W. Bauer, C. Berggren, F. J. Tackmann and J. R. Walsh, *Drell-Yan production at NNLL+NNLO matched to parton showers*, Phy. Rev. D **92** (2015), ISSN: 1550-2368, URL: http://dx.doi.org/10.1103/PhysRevD.92.094020 (cit. on p. 2).

[5] M. A. Ebert, J. K. L. Michel, I. W. Stewart and F. J. Tackmann, *Drell-Yan qT resummation of fiducial power corrections at N3LL*, JHEP **2021** (2021), ISSN: 1029-8479, URL: http://dx.doi.org/10.1007/JHEP04(2021)102 (cit. on p. 2).

[6] W. Bizoń et al., *Fiducial distributions in Higgs and Drell-Yan production at N3LL+NNLO*, JHEP **2018** (2018), ISSN: 1029-8479, URL: http://dx.doi.org/10.1007/JHEP12(2018)132 (cit. on p. 2).

[7] W. Bizoń, P. F. Monni, E. Re, L. Rottoli and P. Torrielli, *Momentum-space resummation for transverse observables and the Higgs p_T at N3LL+NNLO*, JHEP **2018** (2018), ISSN: 1029-8479, URL: http://dx.doi.org/10.1007/JHEP02(2018)108 (cit. on p. 2).

[8] CMS Collaboration, *Angular coefficients of Z bosons produced in pp collisions at $\sqrt{s} = 8$ TeV and decaying to $\mu^+\mu^-$ as a function of transverse momentum and rapidity*, Phys. Lett. B **750** (2015) 154, arXiv: 1504.03512 [hep-ex] (cit. on pp. 2, 9).

[9] ATLAS Collaboration, *Measurement of the angular coefficients in Z-boson events using electron and muon pairs from data taken at $\sqrt{s} = 8$ TeV with the ATLAS detector*, JHEP **08** (2016) 159, arXiv: 1606.00689 [hep-ex] (cit. on pp. 2, 8, 9).

[10] H. Georgi, D. B. Kaplan and L. Randall, *Manifesting the invisible axion at low energies*, Phys. Lett. B **169** (1986) 73, ISSN: 0370-2693, URL: https://www.sciencedirect.com/science/article/pii/037026938690688X (cit. on p. 2).

[11] S. Carra et al., *Constraining off-shell production of axion-like particles with $Z\gamma$ and WW differential cross-section measurements*, (2021), arXiv: 2106.10085 [hep-ex] (cit. on p. 2).

[12] L3 Collaboration, *Study of the $e^+e^- \to Z\gamma$ process at LEP and limits on triple neutral-gauge-boson couplings*, Phys. Lett. B **597** (2004) 119, arXiv: hep-ex/0407012 [hep-ex] (cit. on p. 2).

[13] DELPHI Collaboration, *Study of triple-gauge-boson couplings ZZZ, ZZγ and Z$\gamma\gamma$ at LEP*, Eur. Phys. J. C **51** (2007) 525, arXiv: 0706.2741 [hep-ex] (cit. on p. 2).

[14] OPAL Collaboration,
Search for trilinear neutral gauge boson couplings in $Z\gamma$ production at $\sqrt{s} = 189$ GeV at LEP,
Eur. Phys. J. C **17** (2000) 553, arXiv: hep-ex/0007016 [hep-ex] (cit. on p. 2).

[15] D0 Collaboration,
$Z\gamma$ production and limits on anomalous $ZZ\gamma$ and $Z\gamma\gamma$ couplings in $p\bar{p}$ collisions at $\sqrt{s} = 1.96$ TeV,
Phys. Rev. **D85** (2012) 052001, arXiv: 1111.3684 [hep-ex] (cit. on p. 2).

[16] D0 Collaboration, *Measurement of the $Z\gamma \to \nu\bar{\nu}\gamma$ Production Cross Section and Limits on Anomalous $ZZ\gamma$ and $Z\gamma\gamma$ Couplings in $p\bar{p}$ Collisions at $\sqrt{s} = 1.96$ TeV*,
Phys. Rev. Lett. **102** (2009) 201802, arXiv: 0902.2157 [hep-ex] (cit. on p. 2).

[17] ATLAS Collaboration,
Measurements of $Z\gamma$ and $Z\gamma\gamma$ production in pp collisions at $\sqrt{s} = 8$ TeV with the ATLAS detector,
Phys. Rev. **D93** (2016) 112002, arXiv: 1604.05232 [hep-ex] (cit. on p. 2).

[18] ATLAS Collaboration, *Measurement of the $Z(\to \ell^+\ell^-)\gamma$ production cross-section in pp collisions at $\sqrt{s} = 13$ TeV with the ATLAS detector*, JHEP **03** (2020) 054, arXiv: 1911.04813 [hep-ex]
(cit. on pp. 2, 7, 9–11, 15, 18).

[19] CMS Collaboration, *Measurement of the $Z\gamma$ production cross section in pp collisions at 8 TeV and search for anomalous triple gauge boson couplings*, JHEP **04** (2015) 164,
arXiv: 1502.05664 [hep-ex] (cit. on p. 2).

[20] E. Bothmann et al., *Event generation with Sherpa 2.2*, SciPost Phys. **7** (2019) 034,
arXiv: 1905.09127 [hep-ph] (cit. on p. 3).

[21] J. Alwall et al., *The automated computation of tree-level and next-to-leading order differential cross sections, and their matching to parton shower simulations*, JHEP **07** (2014) 079,
arXiv: 1405.0301 [hep-ph] (cit. on pp. 3, 4).

[22] P. F. Monni, P. Nason, E. Re, M. Wiesemann and G. Zanderighi,
MiNNLOPS: a new method to match NNLO QCD to parton showers, JHEP **2020** (2020),
ISSN: 1029-8479, URL: http://dx.doi.org/10.1007/JHEP05(2020)143 (cit. on pp. 3, 5).

[23] D. Lombardi, M. Wiesemann and G. Zanderighi,
Advancing MiNNLOPS to diboson processes: $Z\gamma$ production at NNLO+PS, JHEP **2021** (2021),
ISSN: 1029-8479, URL: http://dx.doi.org/10.1007/JHEP06(2021)095
(cit. on pp. 3, 5, 18, 19).

[24] M. Grazzini, S. Kallweit and M. Wiesemann, *Fully differential NNLO computations with MATRIX*,
Eur. Phys. J. C **78** (2018), URL: https://doi.org/10.1140%2Fepjc%2Fs10052-018-5771-7
(cit. on pp. 3, 5).

[25] M. Grazzini, S. Kallweit and D. Rathlev,
Wgamma and Zgamma production at the LHC in NNLO QCD, 2015,
arXiv: 1504.01330 [hep-ph] (cit. on pp. 3, 5).

[26] ATLAS Collaboration, *The ATLAS Experiment at the CERN Large Hadron Collider*,
JINST **3** (2008) S08003 (cit. on p. 3).

[27] ATLAS Collaboration, *The ATLAS Collaboration Software and Firmware*,
ATL-SOFT-PUB-2021-001, 2021, URL: https://cds.cern.ch/record/2767187 (cit. on p. 3).

[28] ATLAS Collaboration, *ATLAS data quality operations and performance for 2015–2018 data-taking*,
JINST **15** (2020) P04003, arXiv: 1911.04632 [physics.ins-det] (cit. on p. 4).

[29] ATLAS Collaboration,
Luminosity determination in pp collisions at $\sqrt{s} = 13$ TeV using the ATLAS detector at the LHC,
ATLAS-CONF-2019-021, 2019, URL: https://cds.cern.ch/record/2677054 (cit. on p. 4).

[30] G. Avoni et al., *The new LUCID-2 detector for luminosity measurement and monitoring in ATLAS*,
JINST **13** (2018) P07017 (cit. on p. 4).

[31] S. Höche, F. Krauss, M. Schönherr and F. Siegert,
A critical appraisal of NLO+PS matching methods, JHEP **09** (2012) 049,
arXiv: 1111.1220 [hep-ph] (cit. on p. 4).

[32] S. Höche, F. Krauss, M. Schönherr and F. Siegert,
QCD matrix elements + parton showers. The NLO case, JHEP **04** (2013) 027,
arXiv: 1207.5030 [hep-ph] (cit. on p. 4).

[33] S. Catani, F. Krauss, R. Kuhn and B. R. Webber, *QCD Matrix Elements + Parton Showers*,
JHEP **11** (2001) 063, arXiv: hep-ph/0109231 (cit. on p. 4).

[34] S. Höche, F. Krauss, S. Schumann and F. Siegert, *QCD matrix elements and truncated showers*,
JHEP **05** (2009) 053, arXiv: 0903.1219 [hep-ph] (cit. on p. 4).

[35] R. D. Ball et al., *Parton distributions for the LHC run II*, JHEP **2015** (2015), ISSN: 1029-8479,
URL: http://dx.doi.org/10.1007/JHEP04(2015)040 (cit. on p. 4).

[36] S. Frixione, *Isolated photons in perturbative QCD*, Phys. Lett. B **429** (1998) 369,
arXiv: hep-ph/9801442 (cit. on p. 4).

[37] R. D. Ball et al., *Parton distributions for the LHC run II*, JHEP **04** (2015) 040,
arXiv: 1410.8849 [hep-ph] (cit. on p. 4).

[38] T. Sjöstrand, S. Mrenna and P. Skands, *A brief introduction to PYTHIA 8.1*,
Comput. Phys. Commun. **178** (2008) 852, arXiv: 0710.3820 [hep-ph] (cit. on p. 4).

[39] P. Nason, *A New method for combining NLO QCD with shower Monte Carlo algorithms*,
JHEP **11** (2004) 040, arXiv: hep-ph/0409146 (cit. on p. 4).

[40] S. Frixione, P. Nason and C. Oleari,
Matching NLO QCD computations with Parton Shower simulations: the POWHEG method,
JHEP **11** (2007) 070, arXiv: 0709.2092 [hep-ph] (cit. on p. 4).

[41] S. Alioli, P. Nason, C. Oleari and E. Re, *A general framework for implementing NLO calculations in shower Monte Carlo programs: the POWHEG BOX*, JHEP **06** (2010) 043,
arXiv: 1002.2581 [hep-ph] (cit. on p. 4).

[42] S. Alioli, P. Nason, C. Oleari and E. Re,
NLO vector-boson production matched with shower in POWHEG, JHEP **07** (2008) 060,
arXiv: 0805.4802 [hep-ph] (cit. on p. 4).

[43] ATLAS Collaboration, *Measurement of the Z/γ^* boson transverse momentum distribution in pp collisions at $\sqrt{s} = 7$ TeV with the ATLAS detector*, JHEP **09** (2014) 145,
arXiv: 1406.3660 [hep-ex] (cit. on p. 4).

[44] H.-L. Lai et al., *New parton distributions for collider physics*, Phys. Rev. D **82** (2010) 074024,
arXiv: 1007.2241 [hep-ph] (cit. on p. 4).

[45] J. Pumplin et al.,
New Generation of Parton Distributions with Uncertainties from Global QCD Analysis,
JHEP **07** (2002) 012, arXiv: hep-ph/0201195 (cit. on p. 4).

[46] T. Sjöstrand et al., *An introduction to PYTHIA 8.2*, Comput. Phys. Commun. **191** (2015) 159, arXiv: 1410.3012 [hep-ph] (cit. on pp. 4, 6).

[47] ATLAS Collaboration, *ATLAS Pythia 8 tunes to 7 TeV data*, ATL-PHYS-PUB-2014-021, 2014, URL: https://cds.cern.ch/record/1966419 (cit. on pp. 4, 6).

[48] K. Melnikov, M. Schulze and A. Scharf, *QCD corrections to top quark pair production in association with a photon at hadron colliders*, Phys. Rev. D **83** (2011), ISSN: 1550-2368, URL: http://dx.doi.org/10.1103/PhysRevD.83.074013 (cit. on pp. 4, 17).

[49] D. de Florian et al., *Handbook of LHC Higgs Cross Sections: 4. Deciphering the Nature of the Higgs Sector*, (2016), arXiv: 1610.07922 [hep-ph] (cit. on p. 4).

[50] ATLAS Collaboration, *Summary of ATLAS Pythia 8 tunes*, ATL-PHYS-PUB-2012-003, 2012, URL: https://cds.cern.ch/record/1474107 (cit. on p. 5).

[51] GEANT4 Collaboration, S. Agostinelli et al., *GEANT4 – a simulation toolkit*, Nucl. Instrum. Meth. A **506** (2003) 250 (cit. on p. 5).

[52] ATLAS Collaboration, *The ATLAS Simulation Infrastructure*, Eur. Phys. J. C **70** (2010) 823, arXiv: 1005.4568 [physics.ins-det] (cit. on p. 5).

[53] S. Alioli, P. Nason, C. Oleari and E. Re, *A general framework for implementing NLO calculations in shower Monte Carlo programs: the POWHEG BOX*, JHEP **06** (2010) 043, arXiv: 1002.2581 [hep-ph] (cit. on p. 5).

[54] S. Dulat et al., *New parton distribution functions from a global analysis of quantum chromodynamics*, Phys. Rev. D **93** (2016) 033006, arXiv: 1506.07443 [hep-ph] (cit. on p. 5).

[55] ATLAS Collaboration, *Performance of electron and photon triggers in ATLAS during LHC Run 2*, Eur. Phys. J. C **80** (2020) 47, arXiv: 1909.00761 [hep-ex] (cit. on pp. 6, 16).

[56] ATLAS Collaboration, *Performance of the ATLAS muon triggers in Run 2*, JINST **15** (2020) P09015, arXiv: 2004.13447 [hep-ex] (cit. on pp. 6, 16).

[57] ATLAS Collaboration, *Electron and photon performance measurements with the ATLAS detector using the 2015–2017 LHC proton–proton collision data*, JINST **14** (2019) P12006, arXiv: 1908.00005 [hep-ex] (cit. on pp. 6, 7, 16).

[58] ATLAS Collaboration, *Muon reconstruction and identification efficiency in ATLAS using the full Run 2 pp collision data set at* $\sqrt{s} = 13$ *TeV*, Eur. Phys. J. C **81** (2021) 578, arXiv: 2012.00578 [hep-ex] (cit. on pp. 6, 7).

[59] ATLAS Collaboration, *Measurement of the inclusive isolated prompt photon cross section in pp collisions at* $\sqrt{s} = 8$ *TeV with the ATLAS detector*, JHEP **08** (2016) 005, arXiv: 1605.03495 [hep-ex] (cit. on pp. 7, 9).

[60] ATLAS Collaboration, *Measurement of the photon identification efficiencies with the ATLAS detector using LHC Run 2 data collected in 2015 and 2016*, Eur. Phys. J. C **79** (2019) 205, arXiv: 1810.05087 [hep-ex] (cit. on p. 7).

[61] M. Cacciari, G. P. Salam and G. Soyez, *The anti-kt jet clustering algorithm*, JHEP (2008) 063, ISSN: 1029-8479, URL: http://dx.doi.org/10.1088/1126-6708/2008/04/063 (cit. on p. 7).

[62] ATLAS Collaboration,
Jet reconstruction and performance using particle flow with the ATLAS Detector,
Eur. Phys. J. C **77** (2017) 466, arXiv: 1703.10485 [hep-ex] (cit. on p. 7).

[63] ATLAS Collaboration, *Jet energy scale and resolution measured in proton–proton collisions at* $\sqrt{s} = 13$ *TeV with the ATLAS detector*, Eur. Phys. J. C **81** (2020) 689,
arXiv: 2007.02645 [hep-ex] (cit. on p. 7).

[64] ATLAS Collaboration, *Performance of pile-up mitigation techniques for jets in* pp *collisions at* $\sqrt{s} = 8$ *TeV using the ATLAS detector*, Eur. Phys. J. C **76** (2016) 581,
arXiv: 1510.03823 [hep-ex] (cit. on pp. 7, 16).

[65] J. C. Collins and D. E. Soper, *Angular Distribution of Dileptons in High-Energy Hadron Collisions*, Phys. Rev. D **16** (1977) 2219 (cit. on p. 8).

[66] ATLAS Collaboration, *Measurement of the inclusive isolated prompt photon cross section in* pp *collisions at* $\sqrt{s} = 7$ *TeV with the ATLAS detector*, Phys. Rev. D **83** (2011) 052005,
arXiv: 1012.4389 [hep-ex] (cit. on p. 9).

[67] ATLAS Collaboration, *Measurements of inclusive and differential fiducial cross-sections of* $t\bar{t}\gamma$ *production in leptonic final states at* $\sqrt{s} = 13$ *TeV in ATLAS*, Eur. Phys. J. C **79** (2019) 382,
arXiv: 1812.01697 [hep-ex] (cit. on p. 11).

[68] G. D'Agostini, *A multidimensional unfolding method based on Bayes' theorem*,
Nucl. Instrum. Methods. Phys. Res. A **362** (1995) 487, ISSN: 0168-9002,
URL: https://www.sciencedirect.com/science/article/pii/016890029500274X
(cit. on p. 16).

[69] ATLAS Collaboration, *Muon reconstruction performance of the ATLAS detector in proton–proton collision data at* $\sqrt{s} = 13$ *TeV*, Eur. Phys. J. C **76** (2016) 292, arXiv: 1603.05598 [hep-ex]
(cit. on p. 16).

[70] ATLAS Collaboration, *Jet energy scale and resolution measured in proton–proton collisions at* $\sqrt{s} = 13$ *TeV with the ATLAS detector*, Eur. Phys. J. C **81** (2021) 689,
arXiv: 2007.02645 [hep-ex] (cit. on p. 16).

[71] J. Butterworth et al., *PDF4LHC recommendations for LHC Run II*,
J. Phys. G: Nucl. Part. Phys. **43** (2016) 023001, ISSN: 1361-6471,
URL: http://dx.doi.org/10.1088/0954-3899/43/2/023001 (cit. on p. 17).

[72] ATLAS Collaboration, *Measurements of* $W^+W^-+ \geq 1$ *jet production cross-sections in* pp *collisions at* $\sqrt{s} = 13$ *TeV with the ATLAS detector*, JHEP **06** (2021) 003, arXiv: 2103.10319 [hep-ex]
(cit. on p. 17).

[73] ATLAS Collaboration, *Measurement of the cross-section of the electroweak production of a* $Z\gamma$ *pair in association with two jets in* pp *collisions at* $\sqrt{s} = 13$ *TeV with the ATLAS detector*,
ATLAS-CONF-2021-038, 2021, URL: https://cds.cern.ch/record/2779171 (cit. on p. 18).

Auxiliary material

Figures from 13 to 20 show the data/MC comparison in the SR using Sherpa 2.2.11 as the signal samples. Statistical and experimental uncertainties are shown. The Sherpa 2.2.11 signal sample is scaled by a factor 1.08 to match the data.
Figures from 21 to 24 show the Migration Matrices in the fiducial phase space for SHERPA 2.2.11 MC.

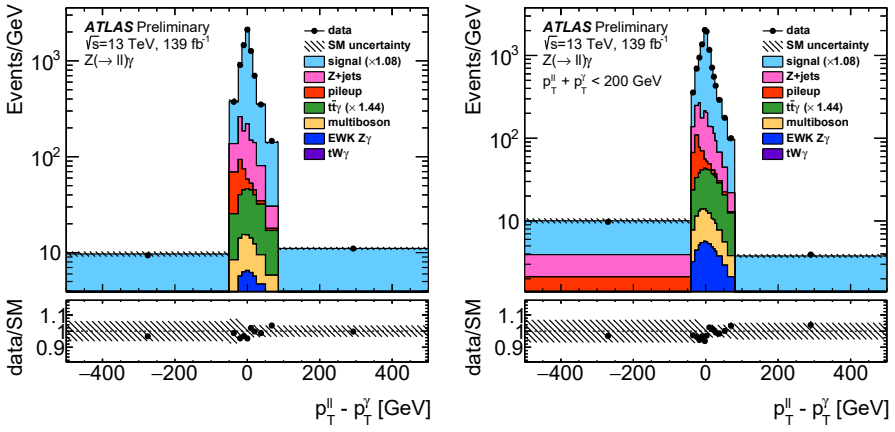

(a) $p_{\mathrm{T}}^{\ell\ell} - p_{\mathrm{T}}^{\gamma}$

(b) $p_{\mathrm{T}}^{\ell\ell} - p_{\mathrm{T}}^{\gamma}$, bin; $p_{\mathrm{T}}^{\ell\ell} + p_{\mathrm{T}}^{\gamma} < 200$ GeV

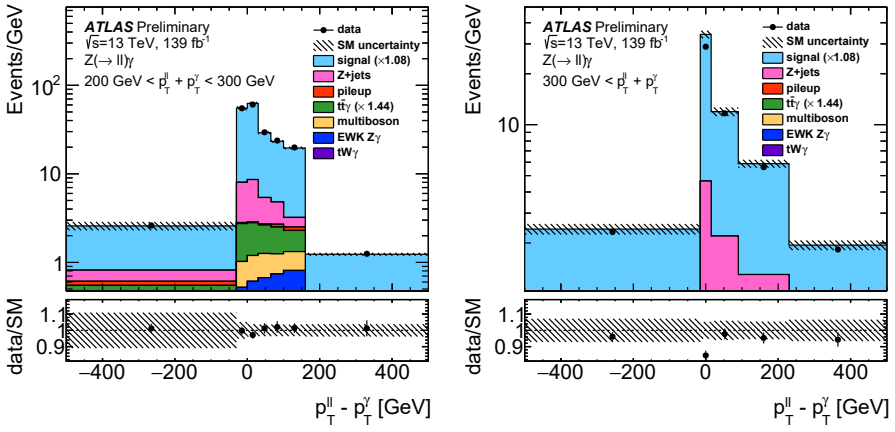

(c) $p_{\mathrm{T}}^{\ell\ell} - p_{\mathrm{T}}^{\gamma}$, bin; 200 GeV $< p_{\mathrm{T}}^{\ell\ell} + p_{\mathrm{T}}^{\gamma} < 300$ GeV

(d) $p_{\mathrm{T}}^{\ell\ell} - p_{\mathrm{T}}^{\gamma}$, bin; $p_{\mathrm{T}}^{\ell\ell} + p_{\mathrm{T}}^{\gamma} > 300$ GeV

Figure 13: Data (black dots) comparison with signal and background estinates in the $ee/\mu\mu\gamma$ channel, for $p_{\mathrm{T}}^{\ell\ell} - p_{\mathrm{T}}^{\gamma}$ (a) inclusively in $p_{\mathrm{T}}^{\ell\ell} + p_{\mathrm{T}}^{\gamma}$, (b) in $p_{\mathrm{T}}^{\ell\ell} + p_{\mathrm{T}}^{\gamma} < 200$ GeV, (c) in 200 GeV $< p_{\mathrm{T}}^{\ell\ell} + p_{\mathrm{T}}^{\gamma} < 300$ GeV, (d) in $p_{\mathrm{T}}^{\ell\ell} + p_{\mathrm{T}}^{\gamma} > 300$ GeV. The bottom panel shows the ratio of observed data to the expectation. The blue band represents the combined systematic uncertainties on the estimates, including the statistical uncertainty. The signal prediction is obtained with Sherpa 2.2.11.

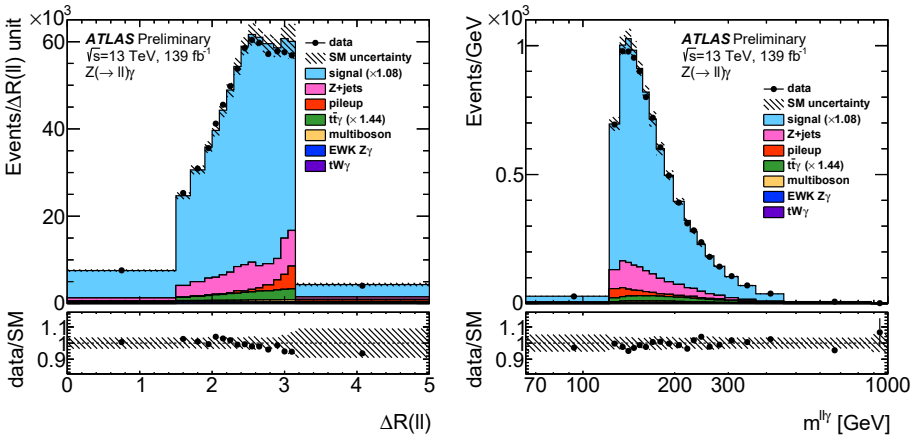

(a) $\Delta R(\ell,\ell)$ (b) $m_{\ell\ell\gamma}$

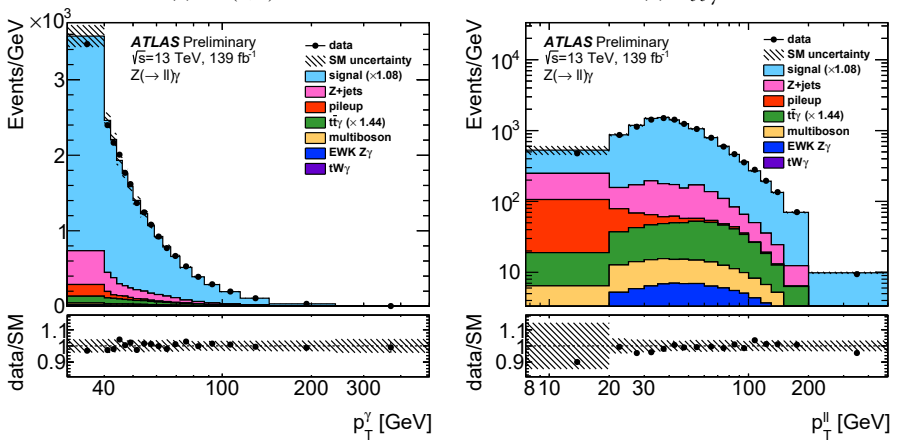

(c) p_{T}^{γ} (d) $p_{\mathrm{T}}^{\ell\ell}$

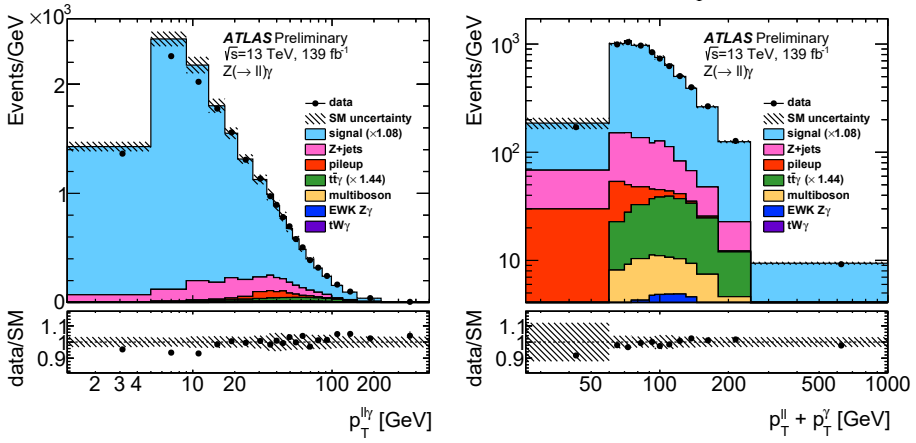

(e) $p_{\mathrm{T}}^{\ell\ell\gamma}$ (f) $p_{\mathrm{T}}^{\ell\ell} + p_{\mathrm{T}}^{\gamma}$

Figure 14: Data (black dots) comparison with signal and background estinates in the $ee/\mu\mu\gamma$ channel, for (a) $\Delta R(\ell,\ell)$, (b) $m_{\ell\ell\gamma}$, (c) p_{T}^{γ}, (d) $p_{\mathrm{T}}^{\ell\ell}$, (e) $p_{\mathrm{T}}^{\ell\ell\gamma}$, and (f) $p_{\mathrm{T}}^{\ell\ell} + p_{\mathrm{T}}^{\gamma}$. The bottom panel shows the ratio of observed data to the expectation. The blue band represents the combined systematic uncertainties on the estimates, including the statistical uncertainty. The signal prediction is obtained with Sherpa 2.2.11.

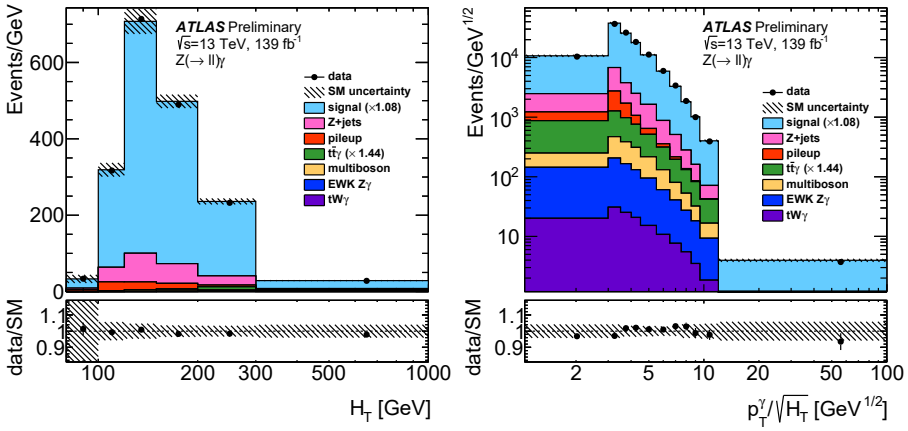

(a) H_{T} (b) $p_{\mathrm{T}}^{\gamma}/\sqrt{H_{\mathrm{T}}}$

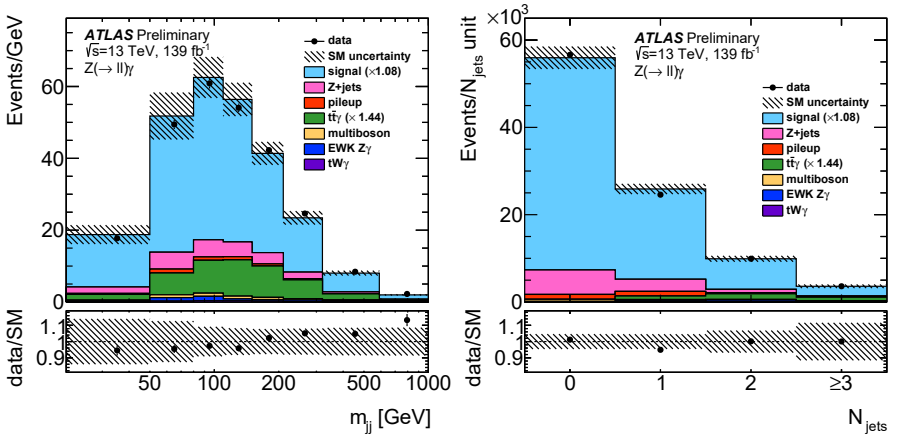

(c) m_{jj} (d) N_{Jet}

Figure 15: Data (black dots) comparison with signal and background estinates in the $ee/\mu\mu\gamma$ channel, for (*a*) H_{T}, (*b*) $p_{\mathrm{T}}^{\gamma}/\sqrt{H_{\mathrm{T}}}$, (*c*) m_{jj}, and (*d*) N_{Jet}. The bottom panel shows the ratio of observed data to the expectation. The blue band represents the combined systematic uncertainties on the estimates, including the statistical uncertainty. The signal prediction is obtained with Sherpa 2.2.11.

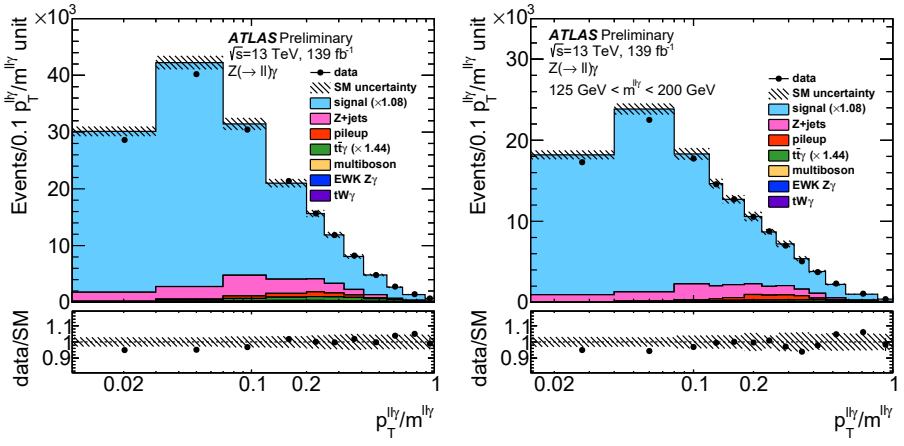

(a) $p_{\mathrm{T}}^{\ell\ell\gamma}/m_{\ell\ell\gamma}$

(b) $p_{\mathrm{T}}^{\ell\ell\gamma}/m_{\ell\ell\gamma}$, bin: 125 GeV $< m_{\ell\ell\gamma} <$ 200 GeV

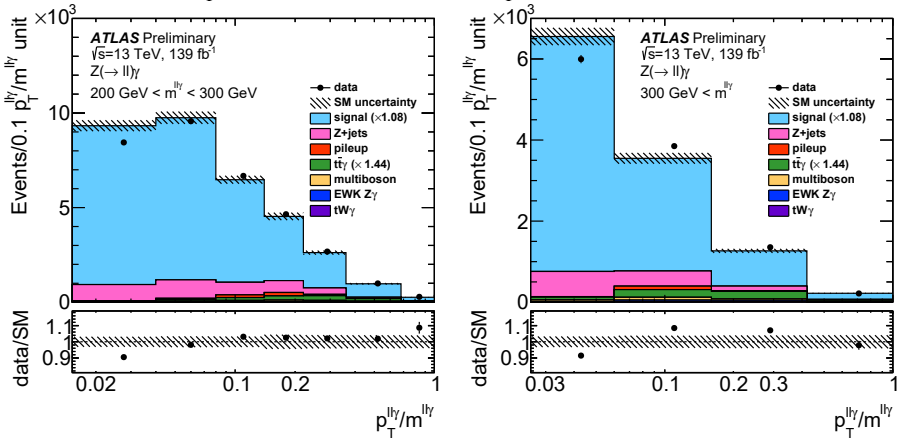

(c) $p_{\mathrm{T}}^{\ell\ell\gamma}/m_{\ell\ell\gamma}$, bin: 200 GeV $< m_{\ell\ell\gamma} <$ 300 GeV

(d) $p_{\mathrm{T}}^{\ell\ell\gamma}/m_{\ell\ell\gamma}$, bin: $m_{\ell\ell\gamma} >$ 300 GeV

Figure 16: Data (black dots) comparison with signal and background estinates in the $ee/\mu\mu\gamma$ channel, for $p_{\mathrm{T}}^{\ell\ell\gamma}/m_{\ell\ell\gamma}$ (*a*) inclusively in $m_{\ell\ell\gamma}$, (*b*) in $m_{\ell\ell\gamma} <$ 200 GeV, (*c*) in 200 GeV $< m_{\ell\ell\gamma} <$ 300 GeV, (*d*) in $m_{\ell\ell\gamma} >$ 300 GeV. The bottom panel shows the ratio of observed data to the expectation. The blue band represents the combined systematic uncertainties on the estimates, including the statistical uncertainty. The signal prediction is obtained with Sherpa 2.2.11.

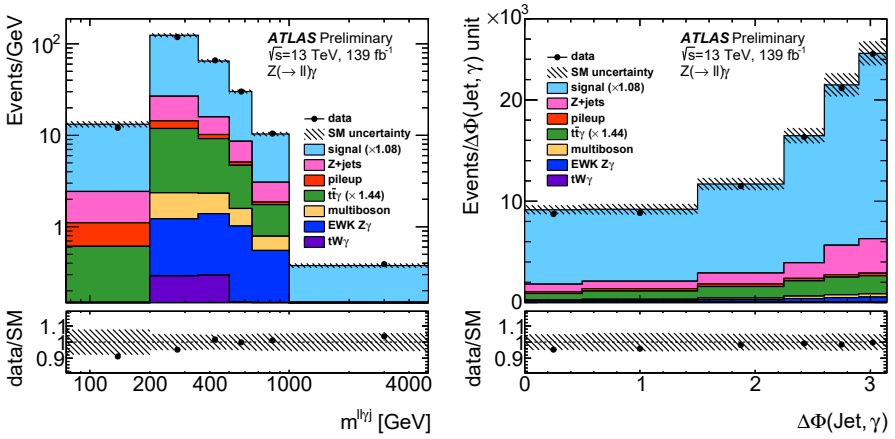

(a) $m_{\ell\ell\gamma j}$

(b) $\Delta\phi(\mathrm{Jet},\gamma)$

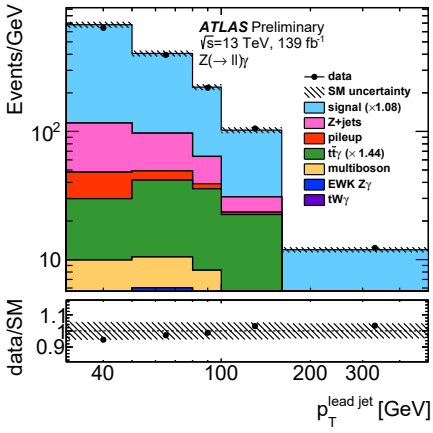

(c) $p_{\mathrm{T}}^{\mathrm{Jet1}}$

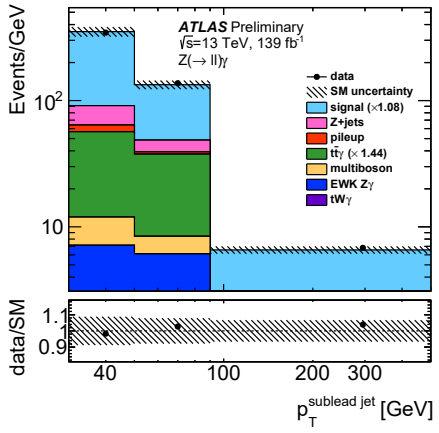

(d) $p_{\mathrm{T}}^{\mathrm{Jet2}}$

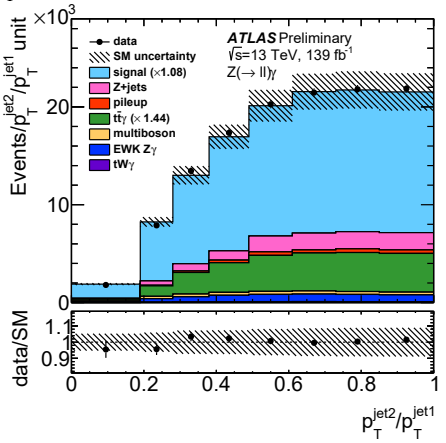

(e) $p_{\mathrm{T}}^{\mathrm{Jet2}}/p_{T}^{\mathrm{Jet1}}$

Figure 17: Data (black dots) comparison with signal and background estinates in the $ee/\mu\mu\gamma$ channel, for (a) $m_{\ell\ell\gamma j}$, (b) $\Delta\phi(\mathrm{Jet},\gamma)$, (c) p_{T}^{Jet1}, (d) p_{T}^{Jet2}, and (e) $p_{\mathrm{T}}^{\mathrm{Jet2}}/p_{T}^{\mathrm{Jet1}}$. The bottom panel shows the ratio of observed data to the expectation. The blue band represents the combined systematic uncertainties on the estimates, including the statistical uncertainty. The signal prediction is obtained with Sherpa 2.2.11.

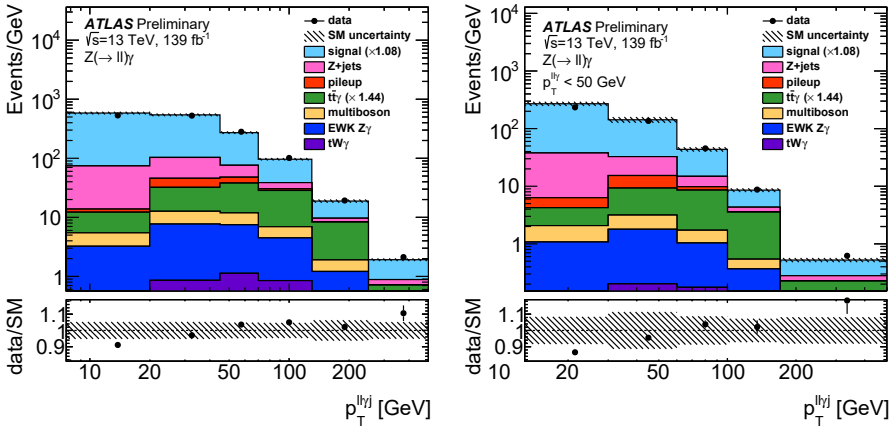

(a) $p_{\mathrm{T}}^{\ell\ell\gamma\mathrm{j}}$

(b) $p_{\mathrm{T}}^{\ell\ell\gamma\mathrm{j}}$, bin: $p_{\mathrm{T}}^{\ell\ell\gamma} < 50$ GeV

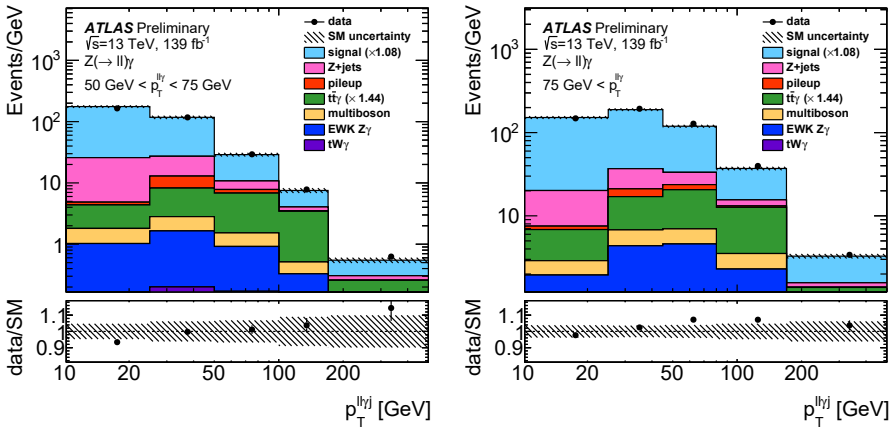

(c) $p_{\mathrm{T}}^{\ell\ell\gamma\mathrm{j}}$, bin: 50 GeV $< p_{\mathrm{T}}^{\ell\ell\gamma} <$ 75 GeV

(d) $p_{\mathrm{T}}^{\ell\ell\gamma\mathrm{j}}$, bin: 75 GeV $< p_{\mathrm{T}}^{\ell\ell\gamma}$

Figure 18: Data (black dots) comparison with signal and background estinates in the $ee/\mu\mu\gamma$ channel, for $p_{\mathrm{T}}^{\ell\ell\gamma\mathrm{j}}$ (a) inclusively in $p_{\mathrm{T}}^{\ell\ell\gamma}$, (b) in $p_{\mathrm{T}}^{\ell\ell\gamma} < 50$ GeV, (c) in 50 GeV $< p_{\mathrm{T}}^{\ell\ell\gamma} <$ 75 GeV, (d) in 75 GeV $< p_{\mathrm{T}}^{\ell\ell\gamma}$. The bottom panel shows the ratio of observed data to the expectation. The blue band represents the combined systematic uncertainties on the estimates, including the statistical uncertainty. The signal prediction is obtained with Sherpa 2.2.11.

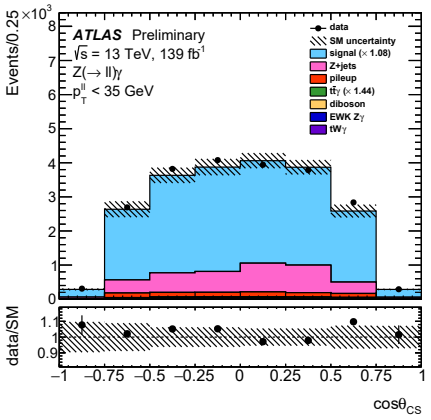

(a) $\cos\theta_{CS}$, bin: $p_{\mathrm{T}}^{\ell\ell} < 35$ GeV

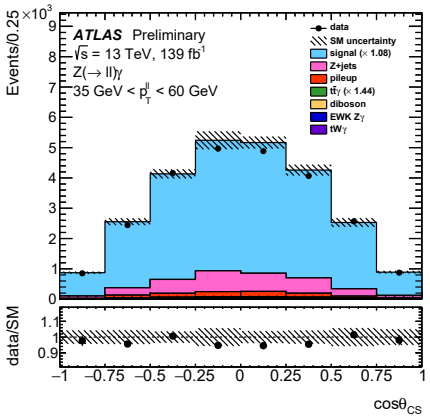

(b) $\cos\theta_{CS}$, bin: 35 GeV $< p_{\mathrm{T}}^{\ell\ell} < 60$ GeV

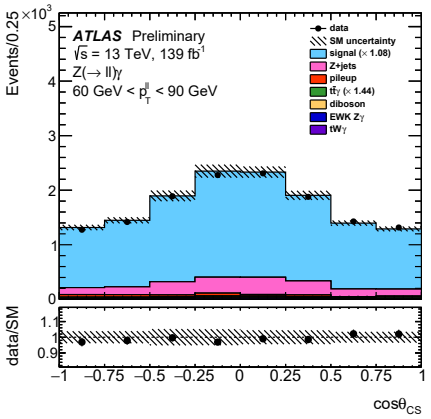

(c) $\cos\theta_{CS}$, bin: 60 GeV $< p_{\mathrm{T}}^{\ell\ell} < 90$ GeV

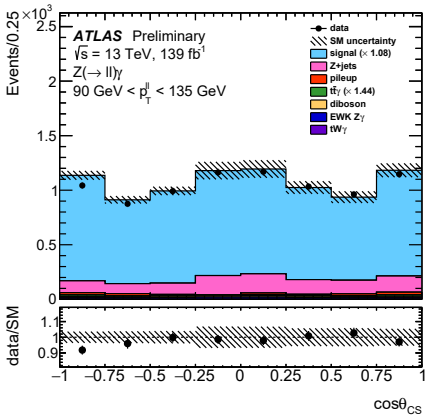

(d) $\cos\theta_{CS}$, bin: 90 GeV $< p_{\mathrm{T}}^{\ell\ell} < 135$ GeV

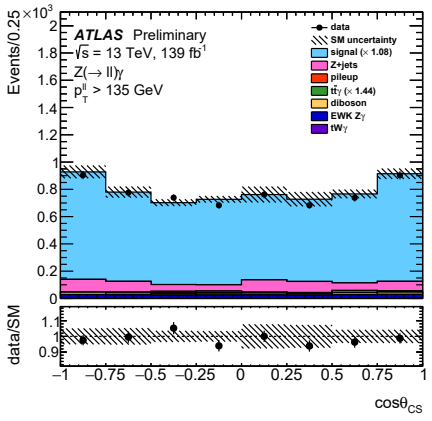

(e) $\cos\theta_{CS}$, bin: 135 GeV $< p_{\mathrm{T}}^{\ell\ell}$

Figure 19: Data (black dots) comparison with signal and background estinates in the $ee/\mu\mu\gamma$ channel, for $\cos\theta_{CS}$ in $p_{\mathrm{T}}^{\ell\ell}$ bins: (a) $p_{\mathrm{T}}^{\ell\ell} < 35$ GeV, (b) 35 GeV $< p_{\mathrm{T}}^{\ell\ell} < 60$ GeV , (c) 60 GeV $< p_{\mathrm{T}}^{\ell\ell} < 90$ GeV, (d) 90 GeV $< p_{\mathrm{T}}^{\ell\ell} < 135$ GeV, and (e) 135 GeV $< p_{\mathrm{T}}^{\ell\ell}$. The bottom panel shows the ratio of observed data to the expectation. The blue band represents the combined systematic uncertainties on the estimates, including the statistical uncertainty. The signal prediction is obtained with Sherpa 2.2.11.

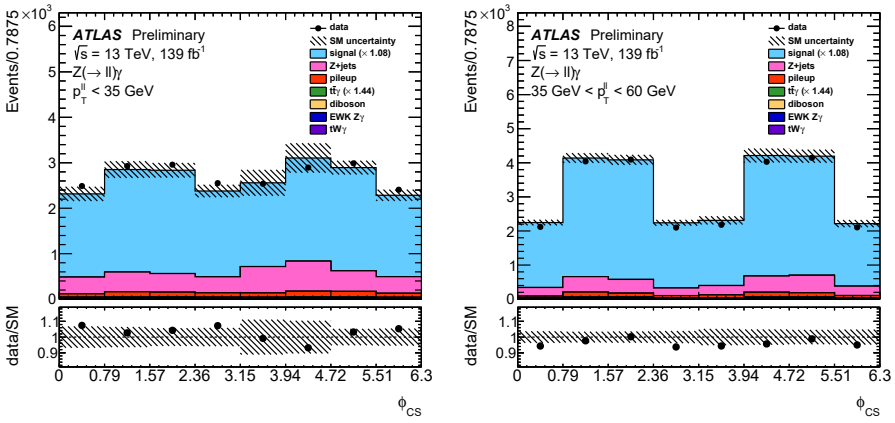

(a) ϕ_{CS}, bin: $p_{\mathrm{T}}^{\ell\ell} < 35$ GeV

(b) ϕ_{CS}, bin: 35 GeV $< p_{\mathrm{T}}^{\ell\ell} < 60$ GeV

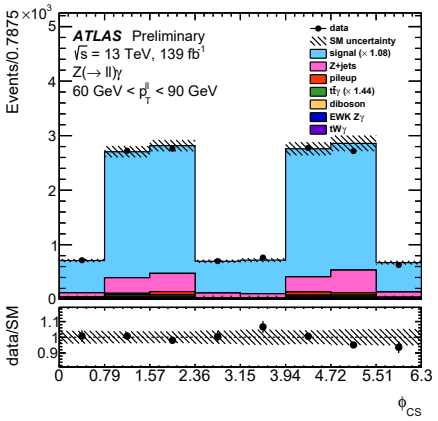

(c) ϕ_{CS}, bin: 60 GeV $< p_{\mathrm{T}}^{\ell\ell} < 90$ GeV

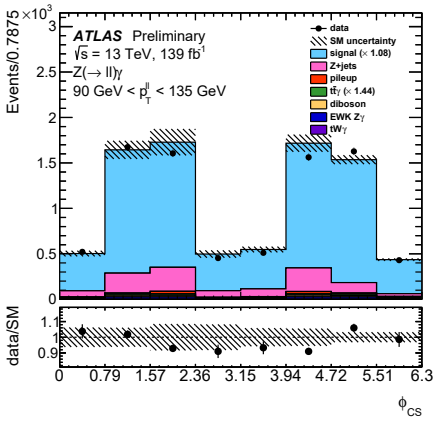

(d) ϕ_{CS}, bin: 90 GeV $< p_{\mathrm{T}}^{\ell\ell} < 135$ GeV

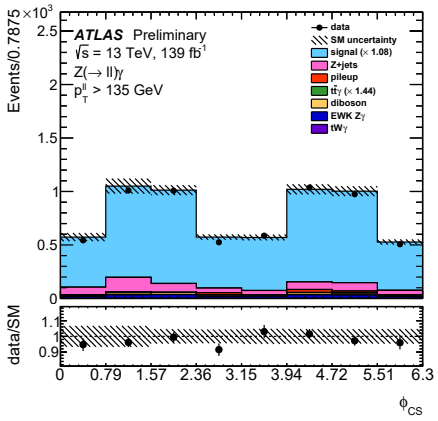

(e) ϕ_{CS}, bin: 135 GeV $< p_{\mathrm{T}}^{\ell\ell}$

Figure 20: Data (black dots) comparison with signal and background estinates in the $ee/\mu\mu\gamma$ channel, for ϕ_{CS} in $p_{\mathrm{T}}^{\ell\ell}$ bins: (a) $p_{\mathrm{T}}^{\ell\ell} < 35$ GeV, (b) 35 GeV $< p_{\mathrm{T}}^{\ell\ell} < 60$ GeV , (c) 60 GeV $< p_{\mathrm{T}}^{\ell\ell} < 90$ GeV, (d) 90 GeV $< p_{\mathrm{T}}^{\ell\ell} < 135$ GeV, and (e) 135 GeV $< p_{\mathrm{T}}^{\ell\ell}$. The bottom panel shows the ratio of observed data to the expectation. The blue band represents the combined systematic uncertainties on the estimates, including the statistical uncertainty. The signal prediction is obtained with Sherpa 2.2.11.

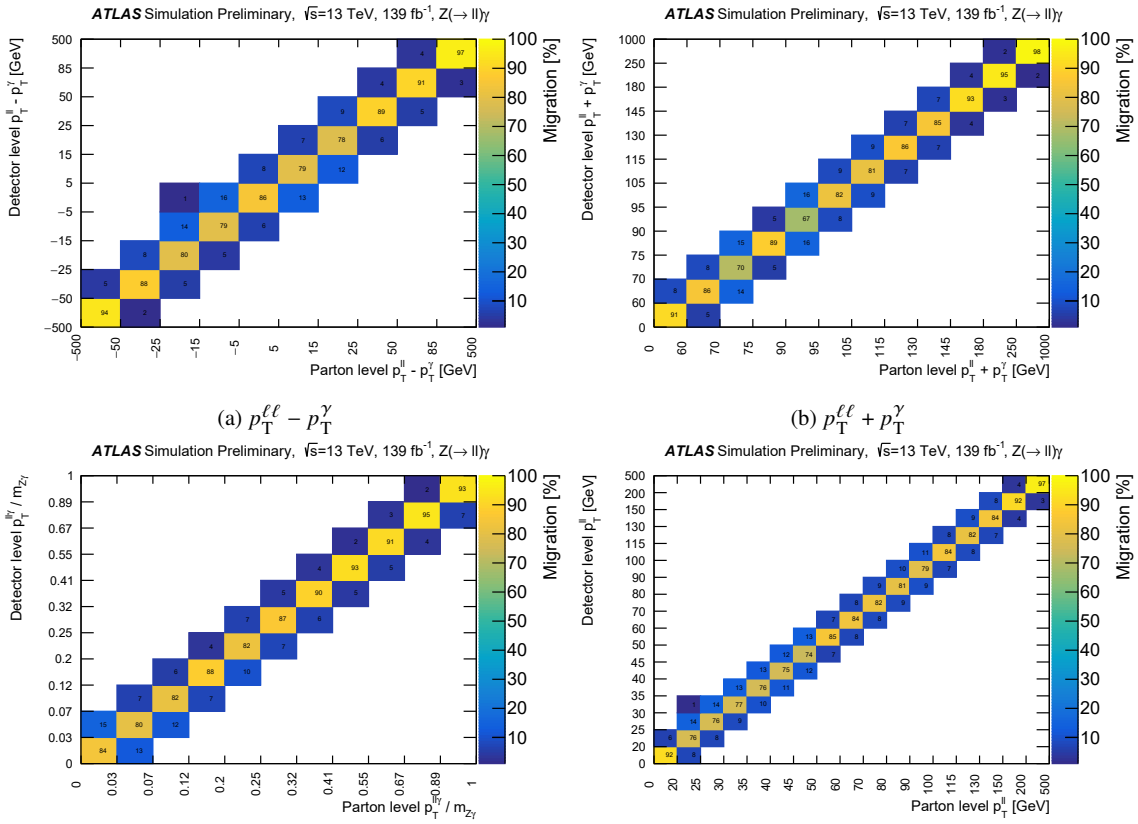

(a) $p_{\mathrm{T}}^{\ell\ell} - p_{\mathrm{T}}^{\gamma}$

(b) $p_{\mathrm{T}}^{\ell\ell} + p_{\mathrm{T}}^{\gamma}$

(c) $p_{\mathrm{T}}^{\ell\ell\gamma}/m_{\ell\ell\gamma}$

(d) $p_{\mathrm{T}}^{\ell\ell}$

Figure 21: Migration Matrices in the fiducial phase space using SHERPA 2.2.11 MC, for (*a*) $p_{\mathrm{T}}^{\ell\ell} - p_{\mathrm{T}}^{\gamma}$, (*b*) $p_{\mathrm{T}}^{\ell\ell} + p_{\mathrm{T}}^{\gamma}$, (*c*) $p_{\mathrm{T}}^{\ell\ell\gamma}/m_{\ell\ell\gamma}$, and (*d*) $p_{\mathrm{T}}^{\ell\ell}$.

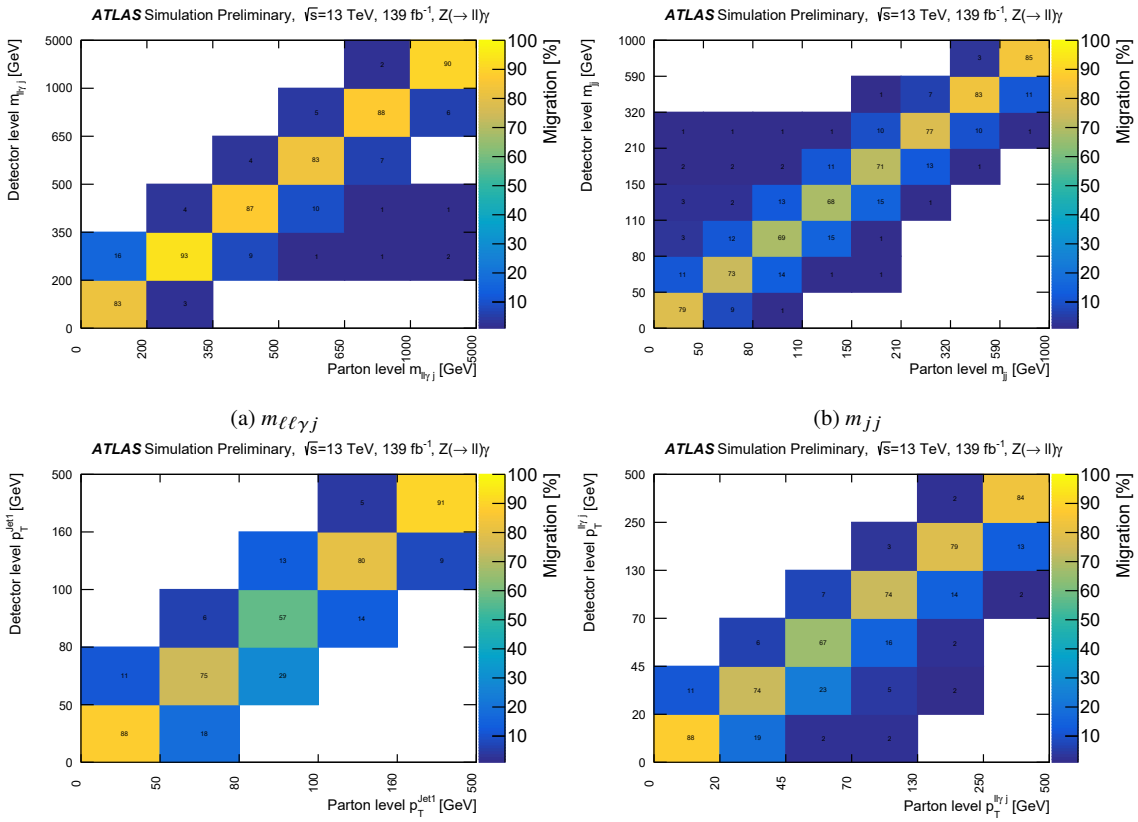

(a) $m_{\ell\ell\gamma j}$

(b) m_{jj}

(c) p_{T}^{Jet1}

(d) $p_{\mathrm{T}}^{\ell\ell\gamma\mathrm{j}}$

Figure 22: Migration Matrices in the fiducial phase space using SHERPA 2.2.11 MC, for (*a*) $m_{\ell\ell\gamma j}$, (*b*) m_{jj}, (*c*) $p_{\mathrm{T}}^{\mathrm{Jet1}}$, and (*d*) $p_{\mathrm{T}}^{\ell\ell\gamma\mathrm{j}}$.

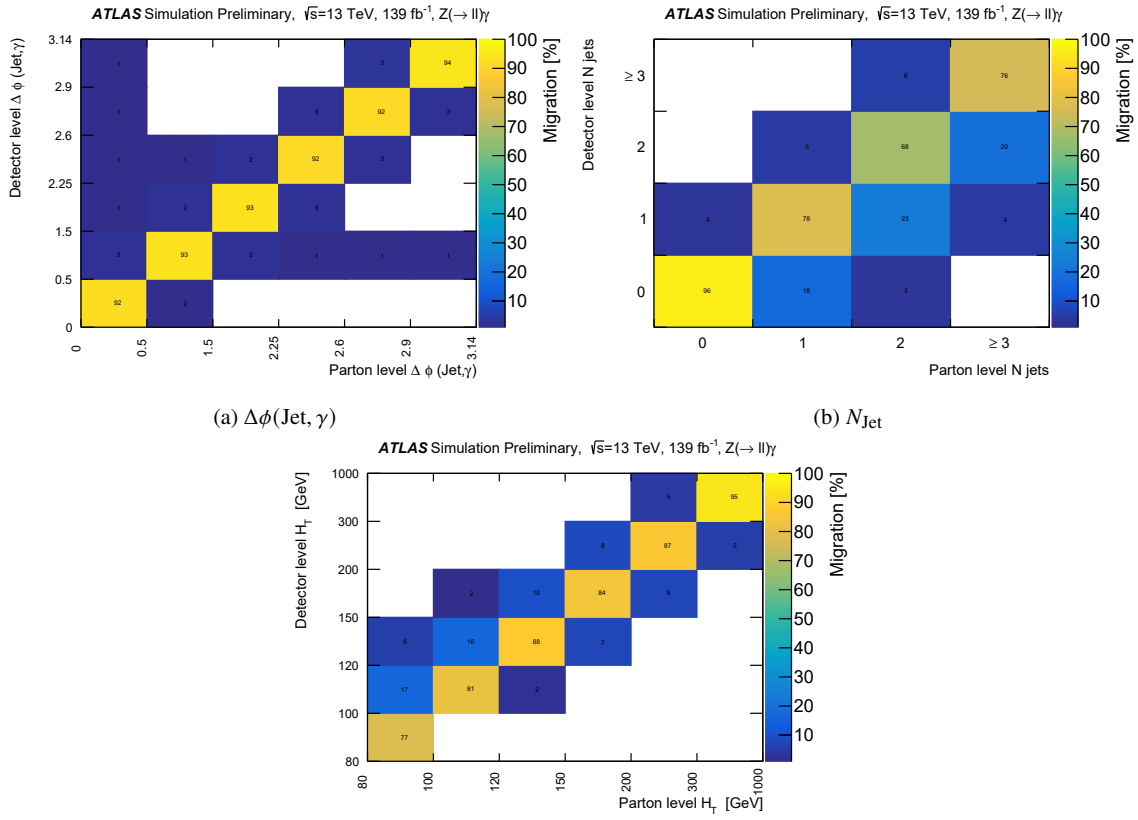

(a) $\Delta\phi(\text{Jet}, \gamma)$ (b) N_{Jet}

(c) H_{T}

Figure 23: Migration Matrices in the fiducial phase space using SHERPA 2.2.11 MC, for (*a*) $\Delta\phi(\text{Jet}, \gamma)$, (*b*) N_{Jet}, and (*c*) H_{T}.

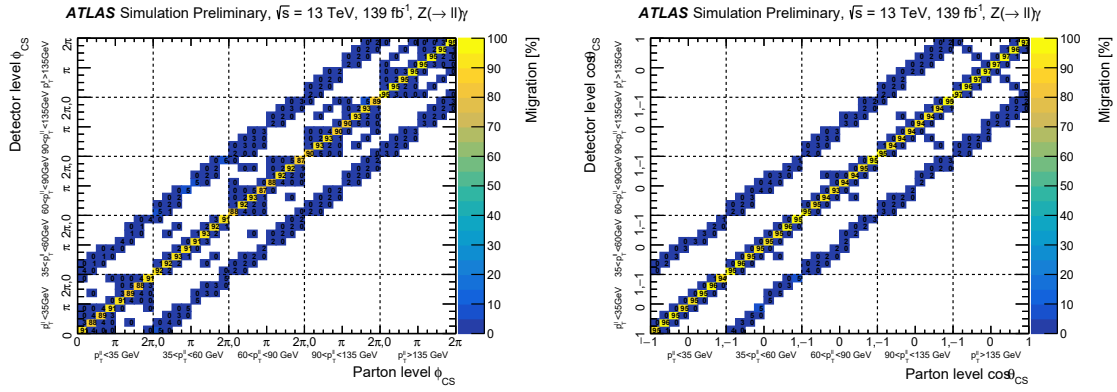

(a) ϕ_{CS} (b) $\cos\theta_{CS}$

Figure 24: Migration Matrices in the fiducial phase space using SHERPA 2.2.11 MC, for (*a*) ϕ_{CS} and (*b*) $\cos\theta_{CS}$.